Test of lepton flavour universality using hadronic tau decays with the LHCb detector

Emmanuel Arbouch

Stage 2016-2017
Master 2 "Sciences de la Matière", mention "Physique, concepts et applications"
École Normale Supérieure de Lyon - Université Claude Bernard Lyon 1

Abstract

The goal of this internship was to realize a preliminary study on the measurement of the $R(D^*)$ parameter, defined as the ratio between the two branching fractions $R(D^*) \equiv \mathcal{B}(B^0 \to D^{*-}\tau^+\nu_\tau)/\mathcal{B}(B^0 \to D^{*-}\mu^+\nu_\mu)$, using the $\tau^+ \to \pi^+\pi^-\pi^+\overline{\nu}_\tau$ hadronic decays recorded by the LHCb detector. The world average on the measurements done so far shows a discrepancy of 3.4 standard deviations with respect to the Standard Model prediction. This points towards Lepton Flavor Universality Violation and needs to be investigated further. So far, the Run 2 (2015-2018) data had never been exploited for the measurement of $R(D^*)$ and a first look was made during this internship. Between Run 1 (2011-2012) and Run 2, the LHC center-of-mass energy increased and the LHCb trigger was improved. Lower statistical error is expected on measurements performed on Run 2 data. The gain in performance due to the improved trigger is evaluated to be 15.3%. Finally, the gain factor brought by Run 2 enhancements to event yields is evaluated to be 5.0 ± 0.2, so that the statistical error on future measurements of the $R(D^*)$ parameter with the LHCb detector would decrease from 6.7% to 3.0%.

Keywords : Lepton Flavour Universality, Semileptonic decay, LHC, LHCb

Supervisor : **Olivier Leroy**
DR - Aix-Marseille Université, CNRS/IN2P3, CPPM, Marseille, France
Olivier.Leroy@cppm.in2p3.fr / tél. (+33) 4 91 82 76 05
163 Avenue de Luminy, case 902, 13288 Marseille Cedex 09
https://www.cppm.in2p3.fr/

Contents

Acknowledgements

I wish to thank Olivier for sharing all these discussions with me throughout the internship. Since the very first minute, he took me straight into the eye of the $R(D^*)$ tornado with passion and expertise. In spite of the additional workload that he has to carry as the leader of the LHCb team in Marseille, he has always been available for inspired guidance. He took all the necessary time to help me settling down within the computing environment at CPPM, sharing good practises with me, so that I could be autonomous very quickly. Whenever I had a technical issue, I never felt isolated very long thanks to him and to all the members of the team : Justine, Giampiero, Julien, Andrey, Krystof, Cedric, Joan and Morgan. I send specific greetings to Krystof, Julien and Joan for their invaluable help while I was discovering the insides of the ROOT, DAVINCI and ROOFIT machineries. I also wish to thank all the Run 1 team, Guy, Concezio, Antonio, Benedetto, Federico and Victor, for their friendly help throughout my internship, and I am grateful for the attention they paid to my preliminary exploration of Run 2 datasets. I wish to thank Andrey for our discussion on the BSM models for $R(D^*)$. To Dawid, who will perform the Run 2 measurement of $R(D^*)$, I wish good luck and at least five sigmas. I would like to thank the heads of the Master 2 “Sciences de la Matière” at the ENS of Lyon, Denis Bartolo and François Gieres, for their availability, their guidance and their attention to all my questions throughout the year. I am grateful to the members of my jury, François Gieres, Gérald Grenier and Alexandre Arbey for their time spent in the assessment of this work, and to all the teachers of the Master for their teaching. Finally, I am indebted to all the members of my family, who supported me during my studies. In particular to my parents, who made this possible.

1 Introduction

Within the Standard Model (SM) of particle physics, Lepton Flavour Universality (LFU) is an accidental symmetry that might be broken only by Yukawa interactions, so that the cross-sections of flavour-changing leptonic processes are identical up to the lepton masses. The value of the W and Z bosons coupling constants, which have been measured precisely during the LEP, SLC and Tevatron era, are compatible with LFU, except from a discrepancy of 2.8 standard deviations in the $\mathcal{B}\ (W^+ \to \tau^+\nu_\tau)/\mathcal{B}\ (W^+ \to e^+(\mu^+)\nu_e(\nu_\mu))$ ratio [a] [1]. This discrepancy points towards Lepton Flavour Universality Violation (LFUV), and theories explaining this phenomenon go beyond the standard model (BSM). Obviously, there is a need to investigate on this discrepancy and to look for confirmations of LFUV through other channels. The observation of LFUV at a high level of significance and in several decay modes would be a clear sign of new physics.
Various searches have been performed in this quest for LFUV observation. Among these, the semileptonic decay $B^0 \to D^{*-}\tau^+\nu_\tau$ has been the object of extensive research for several years. In experimental particle physics, semileptonic decays offer at least three advantages with respect to the other decay modes. First, they only involve tree-level phenomena, which allows to compute very precise SM predictions. Secondly, these decays have a high branching ratio and are easily accessible with the current accelerators. A third advantage is that semileptonic decays having a tau lepton in their final states offer, because of its high mass, a good sensitivity to new physics.
The $R(D^*)$ parameter is defined as

$$R(D^*) \equiv \frac{\mathcal{B}(B^0 \to D^{*-}\tau^+\nu_\tau)}{\mathcal{B}(B^0 \to D^{*-}\ell^+\nu_\ell)}$$

where $\ell^+ = (e^+,\ \mu^+)$ and $\nu_\ell = (\nu_e,\ \nu_\mu)$. In this parameter, the numerator and the denominator depend on the charged leptons only through their masses. When computing this value, most of the uncertainties due to hadronic effects cancel out. This makes the $R(D^*)$ parameter a very sensitive probe to new physics effects. Also, because of the important mass difference between the tau and the two other leptons, the SM prediction for $R(D^*)$ is lower than one [2] :

$$R(D^*)_{\rm SM} = 0.252 \pm 0.003$$

In 2012, the BaBar collaboration measured the $R(D^*)$ parameter [3] :

$$R(D^*)[\text{BaBar 2012}] = 0.332 \pm 0.024\,(\text{stat}) \pm 0.018\,(\text{syst})$$

This measeurement yields a discrepancy at the level of 3 standard deviations with respect to the SM prediction. The Belle and LHCb collaborations performed their own measurements of $R(D^*)$ in 2015 [4, 5], 2016 [6] and 2017[b] [7, 8]. Combined with the $R(D)$ parameter[c] [3, 4], this discrepancy reaches the level of 4.1 standard deviations (figure 1).

[a] Charge conjugation is implied throughout this text.

[b] A short description of the latest result obtained by LHCb on June 6^{th} is available on the LHCb public page : http://lhcb-public.web.cern.ch/lhcb-public/

[c] The ratio $R(D)$ is defined as

$$R(D) \equiv \frac{\mathcal{B}(B0 \to D^-\tau^+\nu_\tau)}{\mathcal{B}(B0 \to D^-\ell^+\nu_\ell)}$$

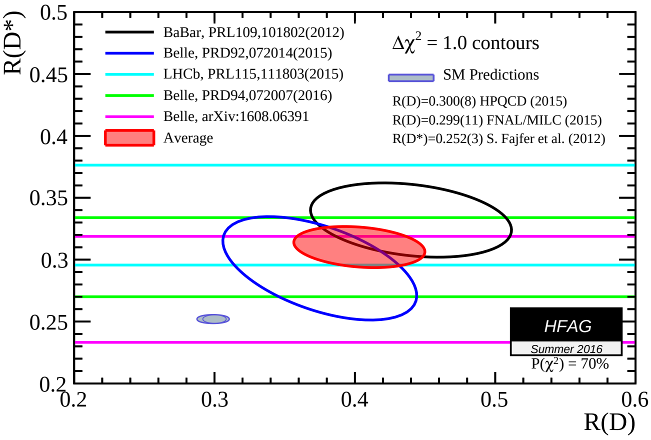

Figure 1: Combined measurements of $R(D)$ and $R(D^*)$ as of Summer 2016. The values predicted by SM theory are represented by the blue-grey ellipse at the bottom left of the plot. Source : Heavy Flavour Averaging Group [9].

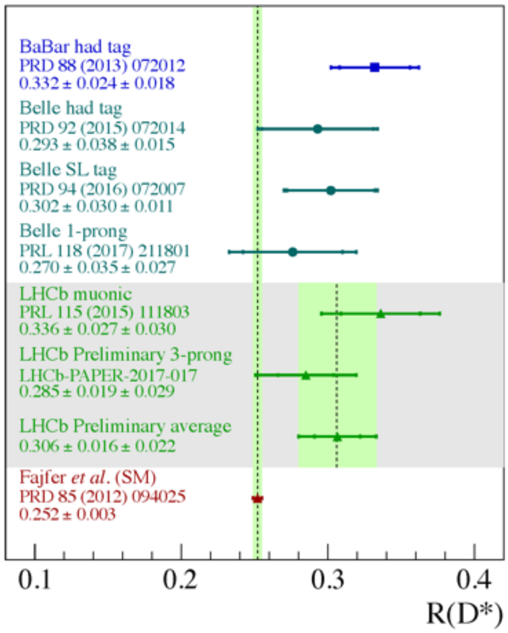

Figure 2: Summary of the $R(D^*)$ measurements performed so far. The value at the bottom (red) is the SM theoretical prediction [2]. Source : LHCb public website.

One can notice that all the measurements of $R(D^*)$ lie above the SM prediction. If the current measured world average was to be confirmed, then 21% of the $B^0 \to D^{*-}\tau^+\nu_\tau$ decays would be mediated by new physics mechanisms. The $R(D^*)$ discrepancy created a tremendous excitation in the community and has generated a lot of interest among theorists [10–13].

The 2017 LHCb measurement will be performed again on Run 2 data (2015-2018), for which the overall performance of LHCb is expected to increase thanks to several improvements made to the detector, and notably to the trigger system. In order to use Run 2 data, which has never been used for this measurement yet, a preliminary study of the method applied on Run 1 data is required. The goal of this internship was to understand the main features of Run 1 measurement, to reproduce them and to use, for the first time, several Run 2 datasets to produce an estimation of the gain that should be brought by the whole Run 2 dataset, which is currently being recorded by the LHCb detector.
This report is organized as follows : a phenomenological description of the $B^0 \to D^{*-}\tau^+\nu_\tau$ decay and an historical overview of the measurement techniques of $R(D^*)$, including the one that will be used on Run 2 data, are presented in Section 2. The LHC and the LHCb detector are presented in Section 3. The study of $B^0 \to D^{*-}\ell^+\nu_\ell$ decays is presented in Section 4. This includes a description of the signal, normalization and main background modes as well as the selection criteria (Section 4.1), the description of new Monte-Carlo (MC) samples that were produced and validated during the internship (Section 4.2), a study of the gain in efficiency brought by the Run 2 trigger system (Section 4.3) and the measurement of the improvements on background and normalization yields (Section 4.4).

2 Phenomenology and world overview of measurements involving semileptonic $B^0 \to D^{*-}\tau^+\nu_\tau$ decays

2.1 Phenomenology of $B^0 \to D^{*-}\tau^+\nu_\tau$ decays

The semileptonic $B^0 \to D^{*-}\tau^+\nu_\tau$ decay belongs to a broader category of $b \to c\tau^-\overline{\nu}_\tau$ transitions that can be described by an effective hamiltonian $\mathcal{H}_{\text{eff}}$ including both SM and BSM contributions :

$$\mathcal{H}_{\text{eff}} = \frac{4G_F}{\sqrt{2}} V_{cb} \left[(1 + C_{V_1})\mathcal{O}_{V_1} + C_{V_2}\mathcal{O}_{V_2} + C_{S_1}\mathcal{O}_{S_1} + C_{S_2}\mathcal{O}_{S_2} + C_T\mathcal{O}_T\right] \tag{1}$$

Where G_F is the Fermi constant and $\mathcal{O}_{V_1}$, $\mathcal{O}_{V_2}$, $\mathcal{O}_{S_1}$, $\mathcal{O}_{S_2}$ and $\mathcal{O}_T$ are the effective vector (V_1, V_2), scalar (S_1, S_2) and tensorial (T) operators :

$$\mathcal{O}_{V_1} = (\bar{c}_L \gamma^\mu b_L)(\bar{\tau}_L \gamma_\mu \nu_L) \tag{2}$$
$$\mathcal{O}_{V_2} = (\bar{c}_R \gamma^\mu b_R)(\bar{\tau}_L \gamma_\mu \nu_L) \tag{3}$$
$$\mathcal{O}_{S_1} = (\bar{c}_L b_R)(\bar{\tau}_L \nu_L) \tag{4}$$
$$\mathcal{O}_{S_2} = (\bar{c}_R b_L)(\bar{\tau}_R \nu_L) \tag{5}$$
$$\mathcal{O}_T = (\bar{c}_R \sigma^{\mu\nu} b_L)(\bar{\tau}_R \sigma_{\mu\nu} \nu_L) \tag{6}$$

And C_{V_1}, C_{V_2}, C_{S_1}, C_{S_2} and C_T are the associated Wilson coefficients. The additional $\mathcal{O}_{V_1}$ operator accounts for the chiral SM term, where the transition is mediated by a W boson (Figure 3, left). It is possible to relate this model-independent effective hamiltonian with other models that involve specific non-SM particles. Among those, the Two-Higgs Doublet Models (2HDM) and Leptoquark (LQ) model can be noticed (Figure 3, resp. center and right). The type-III 2HDM can explain $R(D)$ and $R(D^*)$ simultaneously [10], but type-II 2HDM is disfavoured by the BaBar measurements at the level of 99.8% confidence level [14]. A Leptoquark model [13], although controversial, allows to explain simultaneously several anomalies observed in rare decays of B mesons such as $R(D^*)$, $R(D)$, $R(K)$ [15] and P_5' [16]. Explaining all of these discrepancies simultaneously remains challenging.

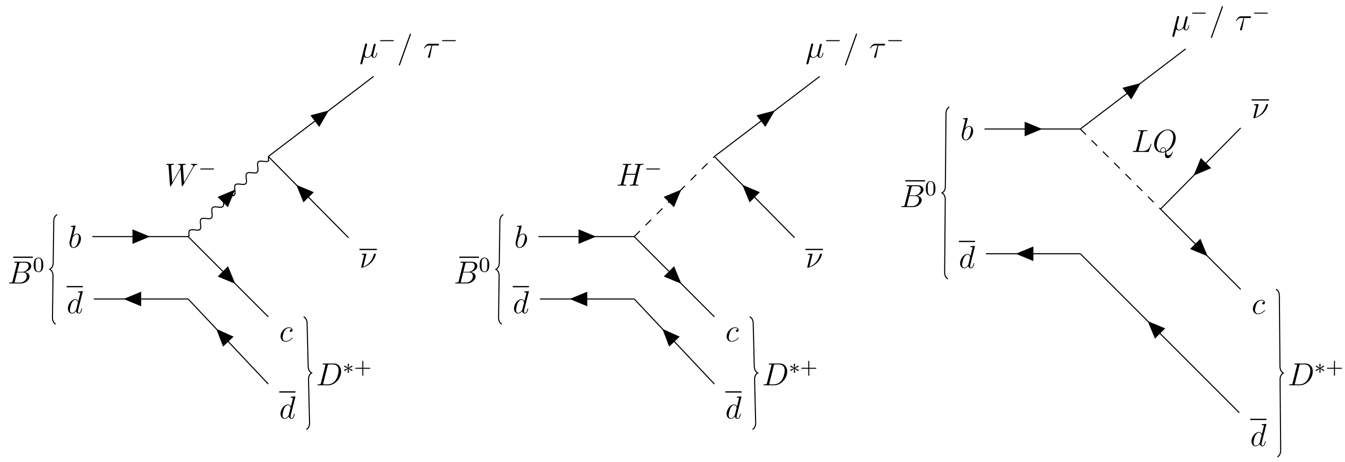

Figure 3: Feynman diagrams of the $B^0 \to D^{*-}\tau^+\nu_\tau$ decay as predicted by the Standard Model (left) and by two BSM models : charged Higgs (center) and Leptoquark (right).

2.2 World overview of measurements involving $B^0 \to D^{*-}\tau^+\nu_\tau$ decays

The measurement of $R(D^*)$ performed by BaBar [3] and Belle [4] respectively in 2012 and 2015 were averaging both electronic and muonic channels. In hadronic detectors, electrons are much more difficult to reconstruct than muons, so that only the muonic channel was used by the LHCb collaboration in 2015 [5]. Besides, the BaBar and Belle measurements fully reconstruct the second B meson decaying into hadronic final states (hadronic tagging), so that the full kinematics of the first B meson decay can be reconstructed despite the presence of neutrinos in its final state. The Belle measurement in 2016 [6] was using a different technique based on a semileptonic decay of the B meson, whereas its 2017 measurement [7] was performed through hadronic tagging and with the tau decaying semi-hadronically *via* the $\tau^+ \to \pi^+\nu_\tau$ and $\tau^+ \to \rho^+\nu_\tau$ modes. The 2017 measurement made by LHCb [8] exploits a fully hadronic mode of the tau lepton, which decays into a three charged particles (prong) channel ($\tau^+ \to \pi^+\pi^-\pi^+(\pi^0)\overline{\nu}_\tau$). A synthesis of the measurements performed so far is presented in Table 1.

Experiment	R_{D^*}	R_D	Re-scaled Correlation
BaBar (2012) [3]	$0.332 \pm 0.024 \pm 0.018$	$0.440 \pm 0.058 \pm 0.042$	-0.27
Belle (2015) [4]	$0.293 \pm 0.038 \pm 0.015$	$0.375 \pm 0.064 \pm 0.026$	-0.49
LHCb (2015) [5]	$0.336 \pm 0.027 \pm 0.030$	–	–
Belle (2016) [6]	$0.302 \pm 0.030 \pm 0.011$	–	–
Belle (2017) [17]	$0.270 \pm 0.035^{+0.028}_{-0.025}$	–	–
LHCb (2017) [8]	$0.285 \pm 0.019 \pm 0.025\,(\text{syst}) \pm 0.013\,(\text{BF})$	–	–
Average	$0.304 \pm 0.013 \pm 0.007$	$0.407 \pm 0.039 \pm 0.024$	-0.20
SM [2, 18]	0.252 ± 0.003	0.299 ± 0.003	

Table 1: Experimental results and SM prediction for the R_{D^*} and R_D parameters. Source : HFLAV [9]

The existing measurements do not allow to clarify the discrepancy observed in $R(D) - R(D^*)$ combined world measurement because of experimental uncertainties. The 2017 LHCb measurement sets a new landmark for these studies, reaching unprecedented statistical precision with a dataset corresponding to an integrated luminosity of $3\,\text{fb}^{-1}$ taken during Run 1 (2011-2012). During the Run 2 phase (2015-2018) the LHC collides protons at higher luminosity with an almost doubled center-of-mass energy (*cf.* Section 3) that also increases the inclusive $b\bar{b}$ production cross-section. However, in the hadronic measurement of $R(D^*)$, the $\tau^+ \to \pi^+\pi^-\pi^+\overline{\nu}_\tau$ decay mode brings additional uncertainties with respect to the leptonic modes, but these partially cancel by introducing a normalization mode that mimics this decay. This is performed as follows : the $R(D^*)$ ratio is redefined by introducing the $B^0 \to D^{*-}\pi^+\pi^-\pi^+$ decay mode :

$$R(D^*) = \frac{\mathcal{B}(B^0 \to D^{*-}\tau^+\nu_\tau)}{\mathcal{B}(B^0 \to D^{*-}\mu^+\nu_\mu)} = \frac{\mathcal{B}(B^0 \to D^{*-}\tau^+\nu_\tau)}{\mathcal{B}(B^0 \to D^{*-}\pi^+\pi^-\pi^+)} \times \frac{\mathcal{B}(B^0 \to D^{*-}\pi^+\pi^-\pi^+)}{\mathcal{B}(B^0 \to D^{*-}\mu^+\nu_\mu)} \tag{7}$$

Since the decays $B^0 \to D^{*-}\tau^+\nu_\tau$ and $\tau^+ \to \pi^+\pi^-\pi^+\overline{\nu}_\tau$ are independent events, it is possible to express the hadronic mode of the tau in terms of these two decays using Bayes' formula :

$$\mathcal{B}(B^0 \to D^{*-}\tau^+\nu_\tau|\tau^+ \to \pi^+\pi^-\pi^+\overline{\nu}_\tau) = \mathcal{B}(B^0 \to D^{*-}\tau^+\nu_\tau) \times \mathcal{B}(\tau^+ \to \pi^+\pi^-\pi^+\overline{\nu}_\tau) \quad (8)$$

So that the $R(D^*)$ parameter can be expressed in terms of the hadronic decay mode of the tau:

$$R(D^*) = \frac{\mathcal{B}(B^0 \to D^{*-}\tau^+\nu_\tau|\tau^+ \to \pi^+\pi^-\pi^+\overline{\nu}_\tau)}{\mathcal{B}(B^0 \to D^{*-}\pi^+\pi^-\pi^+)} \times \frac{\mathcal{B}(B^0 \to D^{*-}\pi^+\pi^-\pi^+)}{\mathcal{B}(B^0 \to D^{*-}\mu^+\nu_\mu)} \times \frac{1}{\mathcal{B}(\tau^+ \to \pi^+\pi^-\pi^+\overline{\nu}_\tau)} \quad (9)$$

The branching fractions $\mathcal{B}$ $(B^0 \to D^{*-}\pi^+\pi^-\pi^+)$, $\mathcal{B}$ $(B^0 \to D^{*-}\mu^+\nu_\mu)$ and $\mathcal{B}$ $(\tau^+ \to \pi^+\pi^-\pi^+\overline{\nu}_\tau)$ have already been measured with relatively good precision [9, 19, 20] :

$$\mathcal{B}(B^0 \to D^{*-}\pi^+\pi^-\pi^+) = (7.21 \pm 0.29).10^{-3} \text{ (4\% precision)} \quad (10)$$

$$\mathcal{B}(B^0 \to D^{*-}\mu^+\nu_\mu) = (4.88 \pm 0.10).10^{-2} \text{ (4\% precision)} \quad (11)$$

$$\mathcal{B}(\tau^+ \to \pi^+\pi^-\pi^+\overline{\nu}_\tau) = (9.31 \pm 0.05).10^{-2} \text{ (<1\% precision)} \quad (12)$$

Therefore the measurement is performed on the $R_{\text{had}}(D^*)$ variable defined as

$$R_{\text{had}}(D^*) \equiv \frac{\mathcal{B}(B^0 \to D^{*-}\tau^+\nu_\tau|\tau^+ \to \pi^+\pi^-\pi^+\overline{\nu}_\tau)}{\mathcal{B}(B^0 \to D^{*-}\pi^+\pi^-\pi^+)} \quad (13)$$

From the experimental point of view, some of the systematic uncertainties cancel in the ratio because the final states are identical in the decay modes on the numerator and on the denominator. The $R_{\text{had}}(D^*)$ parameter can be directly measured by determining the yields and taking into account the efficiency to select the signal $(B^0 \to D^{*-}\tau^+(\to \pi^+\pi^-\pi^+\overline{\nu}_\tau)\nu_\tau)$ and the normalization $(B^0 \to D^{*-}\pi^+\pi^-\pi^+)$ modes :

$$\boxed{R_{\text{had}}(D^*) = \frac{N(B^0 \to D^{*-}\tau^+\nu_\tau|\tau^+ \to \pi^+\pi^-\pi^+\overline{\nu}_\tau)}{N(B^0 \to D^{*-}\pi^+\pi^-\pi^+)} \times \frac{\epsilon_{NORM}}{\epsilon_{SIG}}} \quad (14)$$

3 LHC, LHCb detector and simulation

3.1 LHC

The Large Hadron Collider (LHC) is a proton-proton accelerating and colliding ring-shaped machine with a circumference of 27 kilometers (figure 4). Before entering the LHC, protons are accelerated in a complex made of the Linac, Booster, Proton Synchrotron (PS) and Super Proton Synchrotron (SPS). After circulating through the SPS, the protons are injected into the LHC with a center-of-mass energy $\sqrt{s} = 450\,\text{GeV}$. Two beams are circulating in opposite directions and are accelerated along a circular orbit using RF cavities and superconducting dipole magnets. Additional quadrupole magnets are used to keep the beams focused to increase chances of collision at the interaction points, where the ATLAS, CMS, ALICE and LHCb experiments are installed.
Between 2009 and 2012, the LHC was operating at $\sqrt{s} = 7\,\text{TeV}$ and $8\,\text{TeV}$ (Run 1). Since 2015 and after a one-year shutdown where many improvements were brought to the LHC and to the detectors, the LHC machine has been operating at $\sqrt{s} = 13\,\text{TeV}$ (Run 2). The recording of Run 2 data will last until winter 2018.

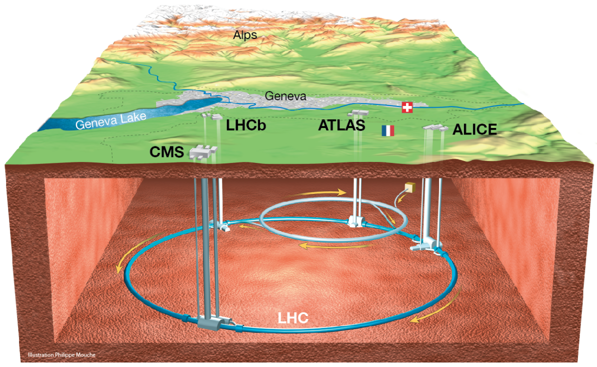

Figure 4: Position of the four main detectors on the LHC ring.

3.2 The LHCb detector

The LHCb detector is a single-arm forward spectrometer installed at Interaction Point 8 of the LHC [21]. It is a single-arm detector because, at high energies, the B and $\overline{B}$ mesons are mostly produced in the same forward or backward cone (figure 6). The detector uses a right-handed Cartesian coordinate system. The z axis is parallel to the beam, the y axis is vertical and the x axis aims towards the center of the LHC. The forward angular coverage of the LHCb detector ranges approximately from 10 to 300 (250) mrad in the bending (non-bending) plane, corresponding to a pseudorapidity range of $1.6 < \eta < 4.9$[d].

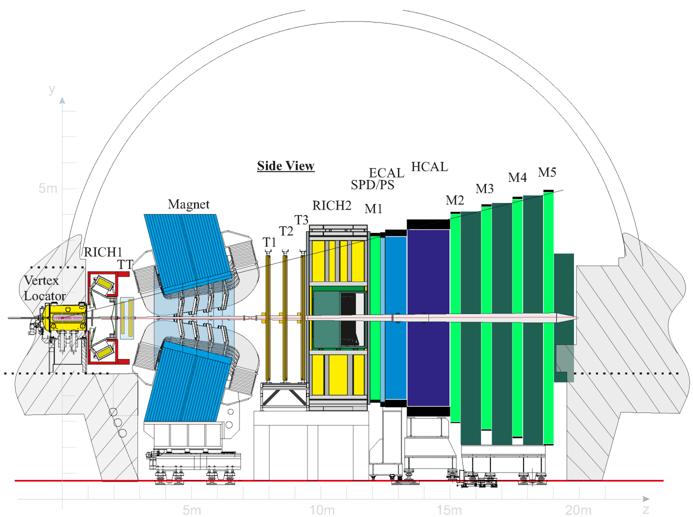

Figure 5: Side view of the LHCb sub-detectors (picture taken from [21])

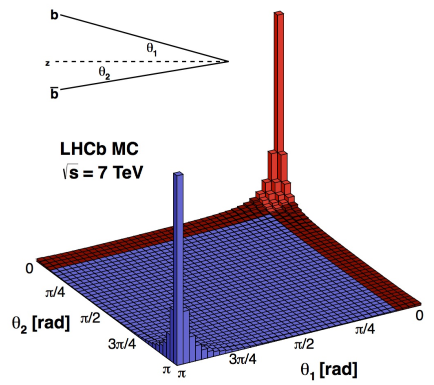

Figure 6: Angular distribution of the $B\overline{B}$ meson production at the LHCb interaction point. The beam line is represented by the z axis (source : University of Heidelberg public website)

The LHCb detector includes a warm dipole magnet which, together with the trajecto-

[d]The pseudorapidity η is a spatial coordinate commonly used in particle physics to describe the angle of a particle with the beam axis. It is defined as $\eta \equiv -\ln\left[\tan\left(\frac{\theta}{2}\right)\right]$, where θ is the angle between the particle three-momentum and the positive direction of the beam axis.

graph, allows to measure the momentum of charged particles passing through the detector. The magnetic field can be oriented either along the positive y direction (*MagUp*) or along the negative one (*MagDown*). It is highly non-homogeneous along the z-axis because of the need to maintain a low-field level inside the RICH sub-detectors, located both upstream and downstream of the magnet (figure 5).

The tracking system has the responsibility to identify tracks and pp primary vertices (PV) while rejecting additional pile-up collisions. This system consists of three main sub-components : the VErtex LOcator (VELO) which is installed around the beam pipe, the Tracker Turicensis (TT) tracking station installed upstream of the magnet and three additional tracking stations (T1-T3) placed downstream of the magnet [22, 23]. The VELO, TT and T1-T3 Inner Tracker are made of silicon miscrostrip detectors, while the T1-T3 Outer Tracker is made of straw-tubes.

The VELO performs high-precision measurements of tracks spatial coordinates close to the interaction region. These tracks are also used to identify the displaced secondary vertices. The sensors of the VELO operate at a small radial distance with respect to the beam. This radial distance is smaller than the aperture required by the LHC during the injection phase, therefore the sensors were designed to be retractable so that they are moved away from the beam pipe during each injection phase.

Many flavour physics analyses, including the one made during this internship, need to distinguish pions from kaons, therefore the LHCb detector relies on an efficient particle identification (PID) system. Exploiting the Cherenkov light emitted by the particles in their active medium, the information provided by the two Ring-Imaging CHerenkov (RICH) detectors allows to identify the passage of charged hadrons [24].

Physics analyses require good reconstruction of π^0 and γ as well as good background rejection with high efficiency. This constrains the quality of both resolution and shower separation powers of the calorimeter system, which consists of an electromagnetic calorimeter (ECAL) followed by a hadronic calorimeter (HCAL) [25].

Muons are present in the final states of many CP-sensitive B decays. They play an important role in CP asymmetry and oscillation measurements. They are both used at the trigger level and for offline analysis. The muon system is composed of 5 rectangular stations (M1-M5) placed along the beam axis [26].

The LHC has been designed to collide protons with an instant luminosity of $\mathcal{L}_{\text{LHC}} = 10^{34}$ cm^2 s^{-1}. The bunch structure of the LHC beam produces bunch crossing at the rate of 40 MHz. In order to reduce radiation damage and pile-up interactions, the nominal luminosity for the LHCb detector has been set to $\mathcal{L}_{\text{LHCb}} = 2 \times 10^{32}$ cm^2 s^{-1}. The visible interactions[e] at LHCb interaction point occur at a rate of 30 MHz, and events are written to storage at the frequency of 5 kHz. The trigger system is responsible for lowering the event frequency from 30 MHz to 5 kHz [27]. Within the LHCb acceptance, only 15% of $b\bar{b}$ events include at least a B meson, plus all its decay products. Since offline analysis applies selections on B meson kinematic quantities (mass, lifetime,*etc.*), the trigger is optimized to achieve high efficiency in B event selection and to reject as many background events as possible. During Run 1 (2009-2012), the trigger consisted of two levels : the first level (L0) and the high level (HLT), divided into HLT1 and HLT2 sub-levels. The event rate was reduced to 1 MHz after L0 trigger and to 5 kHz after HLT (figure 7). The L0 trigger

[e]An interaction is defined to be visible if it produces at least two charged particles with sufficient hits in the VELO and T1T3 to allow them to be reconstructible.

is a hardware stage entirely designed within the LHCb collaboration. It is synchronized with the LHC collision rate to perform “online” selection. The HLT is a software stage implemented on a processor farm made of commercial hardware. It applies asynchronous (“offline”) full event reconstruction before producing a decision.

An additional information step is performed at the trigger level. This information tells whether the decision was due to the signal candidate (“Triggered On Signal”, TOS), to other particles produced in the pp collision (“Triggered Independently of Signal”, TIS), or to a combination of both (“Triggered On Both”, TOB).

The trigger topology has been modified between run 1 (2011-2012) and run 2 (2015-2018), introducing as from 2015 the so-called Turbo stream (figure 8). The hardware stage randomly selects a predefined fraction of all beam-beam crossings at a rate of 300 kHz, then a software stage is applied online. In between the hardware and software stages, an alignment and calibration of the detector is performed in near real-time [28] and updated constants are made available for the trigger. The same alignment and calibration information is propagated to the offline reconstruction, ensuring consistent particle identification information between the trigger and offline software. The identical performance of the online and offline reconstruction allows to perform physics analyses directly using candidates reconstructed in the trigger [27, 29, 30]. The storage of only the triggered candidates enables a reduction in the event size by a factor ten.

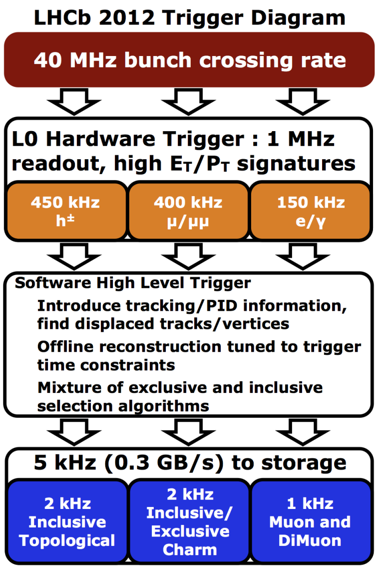

Figure 7: Trigger scheme for Run 1 (source : https://lhcb.web.cern.ch)

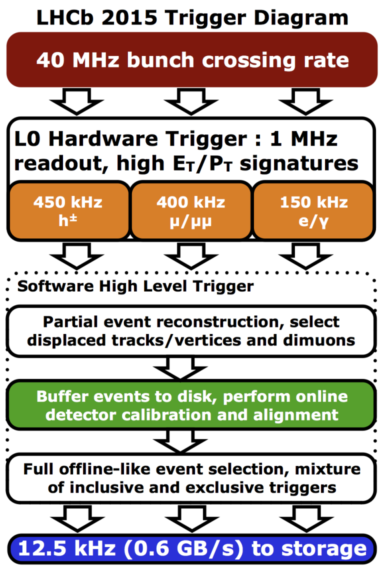

Figure 8: Trigger scheme for Run 2, using real-time alignment and calibration (source : https://lhcb.web.cern.ch)

3.3 Simulation

In the simulation, pp collisions are generated using Pythia [31] with a specific LHCb configuration [32]. Decays of hadronic particles are described by EvtGen [33], in which final-state radiation is generated using Photos [34]. The interaction of the generated particles with the detector, and its response, are implemented using the Geant4 toolkit [35] as described in Ref. [36].

4 Study of $B^0 \to D^{*-}\tau^+(\to \pi^+\pi^-\pi^+\overline{\nu}_\tau)\nu_\tau$ with LHCb

4.1 Description of the signal, normalization and background modes

4.1.1 General description

The $R_{\text{had}}(D^*)$ parameter is defined as the ratio between the branching fraction of $B^0 \to D^{*-}\tau^+\nu_\tau$ decay, with $\tau^+ \to \pi^+\pi^-\pi^+\overline{\nu}_\tau$ (signal mode, Figure 10) and $B^0 \to D^{*-}\pi^+\pi^-\pi^+$ decay (normalization mode, Figure 11). The full decay chains required for signal and normalization candidates are described in Figure 9.
Many decays of the B^0 constitute background modes for this analysis. These backgrounds are described in Table 2.

$$
\begin{aligned}
&B^0 \to D^{*-}\tau^+\nu_\tau \\
&\qquad\qquad \hookrightarrow \pi^+\pi^-\pi^+(\pi^0)\overline{\nu}_\tau \\
&\quad \hookrightarrow \pi^-\overline{D}^0 \\
&\qquad\quad \hookrightarrow K^+\pi^-
\end{aligned}
\qquad\qquad
\begin{aligned}
&B^0 \to D^{*-}\pi^+\pi^-\pi^+(\pi^0) \\
&\qquad \hookrightarrow \pi^-\overline{D}^0 \\
&\qquad\qquad \hookrightarrow K^+\pi^-
\end{aligned}
$$

Figure 9: Full decay chain for signal (left) and normalization (right) candidate events

Signal channel	Branching Fraction (%)
$B^0 \to D^{*-}\tau^+(\to \pi^+\pi^-\pi^+(\pi^0)\overline{\nu}_\tau)\nu_\tau$	0.23 ± 0.03
Normalization channel	$\mathcal{B}$ (%)
$B^0 \to D^{*-}\pi^+\pi^-\pi^+$	0.721 ± 0.029
Background channels	$\mathcal{B}$ (%)
$B^0 \to D^{*-}\pi^+\pi^-\pi^+X$	2.5 ± 0.3
$B^0 \to D^{*-}D_s^+/D_s^{*+}/D_s^+(2317)/D_s^+(2457)(\to \pi^+\pi^-\pi^+X)$	0.56 ± 0.06
$B^0 \to D^{*-}K^+D^{*0}(\to D^0(\to K^-\pi^+\pi^-\pi^+(\pi^0))\gamma/\pi^0)$	0.130 ± 0.012
$B^0 \to D^{*-}K^0D^{*+}(\to D^0(\to K^-\pi^+\pi^-\pi^+(\pi^0))\pi^+)$	0.067 ± 0.006
$B^0 \to D^{*-}D_s^+/D_s^{*+}/D_s^+(2317)/D_s^+(2457)(\to \pi^+\pi^-\pi^+)$	0.040 ± 0.004
$B^0 \to D^{*-}K^+D^0(\to K^-\pi^+\pi^-\pi^+(\pi^0))$	0.030 ± 0.003
$B^0 \to D^{*-}K^0D^+(\to \pi^+\pi^-\pi^+(X))$	0.0123 ± 0.0011
$B^0 \to D^{*-}K^0D^{*+}(\to D^+(\to \pi^+\pi^-\pi^+(\pi^0))\gamma/\pi^0)$	0.0050 ± 0.0005
$B^0 \to D^{*-}D^+(\to \pi^+\pi^-\pi^+(X))$	0.0012 ± 0.0001

Table 2: Branching fractions for signal, normalization and background channels. The value of the branching fractions are taken from [8]

The $B^0 \to D^{*-}D_s^+/D_s^{*+}/D_s^+(2317)/D_s^+(2457)(\to \pi^+\pi^-\pi^+X)$ decay channel represents the most important background for this analysis because it has the highest branching fraction. Also, its topology is very similar to the signal, where both τ and D_s^+ are transported away from the B^0 decay vertex. Hereafter, all background modes

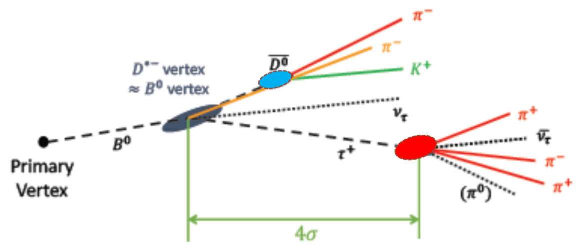

Figure 10: Topology of a signal event : $B^0 \to D^{*-}\tau^+\nu_\tau$ with $\tau^+ \to \pi^+\pi^-\pi^+\overline{\nu}_\tau$ ("Inverted" topology, picture taken from [8])

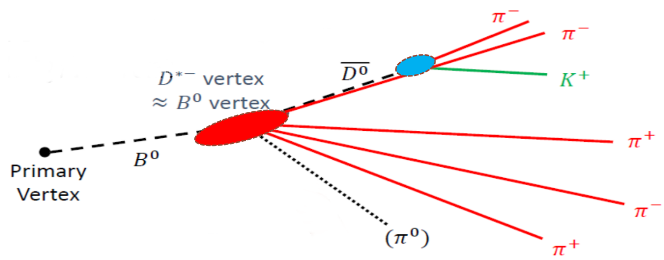

Figure 11: Topology of a normalization event : $B^0 \to D^{*-}\pi^+\pi^-\pi^+$ ("Normal" topology, picture taken from [8])

containing two charm mesons in their decay chain will be referred to as "doubly-charmed" backgrounds.

In all the considered decay modes, the D^* meson refers to the D^* (2010), which is a narrow resonance immediately decaying to $D^0\pi^-$. This allows a powerful cut on the invariant mass difference between the $K\pi\pi$ and the $K\pi$ system. This cut enhances the whole event selection [37]. In practice, the resolution limitations of the LHCb detector do not allow to distinguish the B^0 and D^{*-} decay vertices. Therefore, both vertices are considered to be located at the same spatial point. Still, the measurement is not affected because the final selection does not explicitly require such a discrimination.

4.1.2 Signal and background discrimination

Compared to the leptonic or semileptonic modes of the tau decay, measuring $R(D^*)$ using a fully hadronic decay mode of the tau presents several advantages. First, the normalization channel is chosen so that most of production yield, branching ratio uncertainties and systematics linked to trigger, particle identification and selection cuts cancel out. Secondly, the absence of charged leptons in the final state removes the necessity to separate the signal decay from backgrounds involving electrons or muons such as in semileptonic decays of charmed hadrons. A third advantage is that the kinematics of the event in the B^0 frame can be almost reconstructed. This is because the information missed by the detector due to the presence of two neutrinos in the final state is compensated by the possibility to reconstruct the position of both B^0/τ vertices and directions of flight. Finally, the mass peaks do not come from signal but from backgrounds. This provides an efficient way to control these backgrounds.

However, two major obstacles arise from this choice of decay mode. First, the normalization mode $B^0 \to D^{*-}\pi^+\pi^-\pi^+$ is very close to an important background where additional particles are emitted at the B^0 vertex ($B^0 \to D^{*-}\pi^+\pi^-\pi^+X$), which is approximately 100 times more abundant than signal. This obstacle can be overcome by imposing a simple constrain on the event topology : in signal mode, the τ decay vertex is transported away from the B^0 vertex due to its significant lifetime added to the boost in the forward direction, made possible by the high mass of the B^0. This vertex separation between the B^0 and the τ, hereafter denoted as the "inverted topology", allows to distinguish signal-like topology (Figure 10) from other topologies where the three pions originate from the B^0 vertex, denoted as the "normal topology" (Figures 11 and 12). This method is described in Section 4.1.3. The second obstacle is a consequence of the first one. After applying the selection on inverted topology, the only remaining backgrounds are the doubly-charmed events. In these events a charm carrier is transported away from the B^0 decay vertex, so that these events present the same topology as signal ones. This obstacle is overcome by using the specific features of the tau decay into three pions, by applying neutral isolation criteria to the event and by partially reconstructing the background events. The main features of these techniques are described in Section 4.1.4. Furthermore, the D_s^+, D^0 and D^+ mesons can also decay into three pions. Although the exclusive mode $D_s^+ \to \pi^+\pi^-\pi^+$ has a low branching fraction ($\approx 1\%$), the D_s^+ can also decay into many 3π+X final states (η πX, η' π X, ϕ/ω π X, K^0 3π, η 3π, η' 3π, ω 3π, ϕ 3π, *etc.*), which raises the total branching fraction of $D_s^+ \to 3\pi X$ up to almost 25% [20]. Some of these branching ratios have already been measured (but their precision is variable), some have not. However, most of these backgrounds can be controlled by using specific mass peaks in the 3π mass distribution.

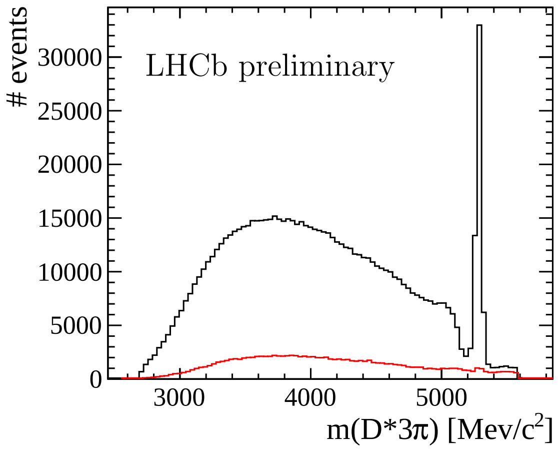

Figure 12: Invariant mass distribution of the D^* 3π system before (black) and after (red) applying the vertex inversion requirement in 2011-2012 datasets. The peak around the B^0 mass (5279.63 MeV/c^2) is due to normalization-like events ($B^0 \to D^{*-}\pi^+\pi^-\pi^+$ and $B^0 \to D^{*-}\pi^+\pi^-\pi^+X$). The vertex inversion requirement strongly reduces the number of events in the peak, giving access mostly to signal-like topologies within the [2750;5000] MeV/c^2 region.

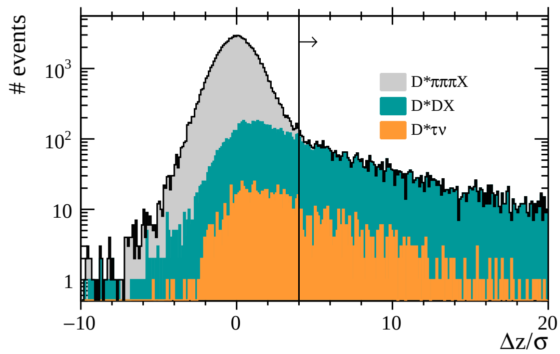

Figure 13: Distribution of the distance, projected on the beam axis, between the τ vertex and the B^0 vertex in units of significance (Δz/σ) in 2011 Monte-Carlo samples. The cut requires this quantity to be greater than four (vertical line). Above this threshold, the normalization-like topologies are highly suppressed whereas signal-like topologies ($B^0 \to D^{*-}\tau^+\nu_\tau$ signal, $B^0 \to D^{*-}D^+$ background) are still present.

4.1.3 Vertex inversion and cleaning cuts

A selection based on the origin of the 3π system is applied to discriminate signal-like topology ("inverted vertex") from normalization-like one. The B^0 decay vertex and the 3π vertex are reconstructed by the detector, then a cut is applied on the difference of the vertices position, projected along the beam axis. This quantity is required to be greater than four times the error on the vertices position (Figures 12 and 13). Additional cuts are applied : the selection requires the event to contain only one B^0 candidate. The projection on the beam axis of the τ flight distance with respect to the primary vertex (PV) is required to be greater than ten times its error, and the cylindrical distance (`BPVVDR`) between its decay vertex and the PV is required to be outside the beam and inside the beam pipe. The $\overline{D}^0$ is required not to be originating from the primary vertex, so a cut on its impact parameter with respect to the PV ($\chi^2[\mathrm{IP}_{\mathrm{PV}}(\overline{D}^0)]$) is applied, and it is required to originate from the same primary vertex as the tau. The analysis needs the τ decay vertex to be well-reconstructed, therefore a good quality on the 3π vertex ($\chi^2[\mathrm{IP}_{\mathrm{PV}}(\pi)]$) is required. This allows to require the quality of the reconstructed tau vertex ($\chi^2[\mathrm{vtx}(\tau^+)]$) to be lower. In order to suppress misidentified kaons, the output (`ProbNNPi`) of a neural network [38] is required to identify particles originating from the τ vertex as pions with a probability higher than 0.6, and to identify the particle originating from the D^{*-} as a pion with a probability higher than 0.1. An additional selection is performed on the difference of masses between the D^{*-} (m = 2010.26 ± 0.05 MeV) and the $\overline{D}^0$ (m = 1864.83 ± 0.05 MeV) candidates. The list of these requirements is summarized in Table 3, and their effect on the several variables in simulated samples are shown on Figure 14.

Variable	**Cut**
$[\mathrm{vtx}_z(B^0) - \mathrm{vtx}_z(\tau^+)]/\mathrm{error}$	< -4
number of B^0 candidates	$= 1$
$[\mathrm{vtx}_z(\tau^+) - \mathrm{vtx}_z(\mathrm{PV})]/\mathrm{error}$	> 10
`BPVVDR`(τ^+)	$[0.2, 0.5]$ mm
$\chi^2[\mathrm{IP}_{\mathrm{PV}}(\overline{D}^0)]$	> 10
$\mathrm{PV}_z(\overline{D}^0)$	$= \mathrm{PV}_z(\tau^+)$
$\chi^2[\mathrm{IP}_{\mathrm{PV}}(\pi)]$, π from τ^+	> 15
$\chi^2[\mathrm{vtx}(\tau^+)]$	< 10
`ProbNNpi` of each π from τ^+	> 0.6
`ProbNNpi` of π from D^{*-}	> 0.1
$\Delta\mathrm{M} = \mathrm{M}(D^{*-}) - \mathrm{M}(\overline{D}^0)$	$[143, 148]\,\mathrm{MeV}/c^2$

Table 3: Summary of the vertex inversion and cleaning requirements [8]

4.1.4 Additional requirements

The vertex inversion and the cleaning cuts described in the previous Section are efficient for suppressing backgrounds where the three pions do not originate from the B^0 decay vertex. But they are not sufficient to suppress backgrounds where the three pions (or several of them) originate from a different vertex, such as the doubly-charmed backgrounds. These additional backgrounds involve one or more additional particles, therefore they can be removed by a multivariate algorithm (Boosted Decision Tree [39]) containing information on the 3π system dynamics ($\min(m_{\pi\pi})$ and $\max(m_{\pi\pi})$), on the B dynamics ($\mathrm{m}(D^*\,3\pi)$), on partially reconstructed backgrounds which do not contain any neutrino and can therefore be reconstructed, as well as on neutral isolation through the analysis of the energy contained in a cone around the 3π direction.

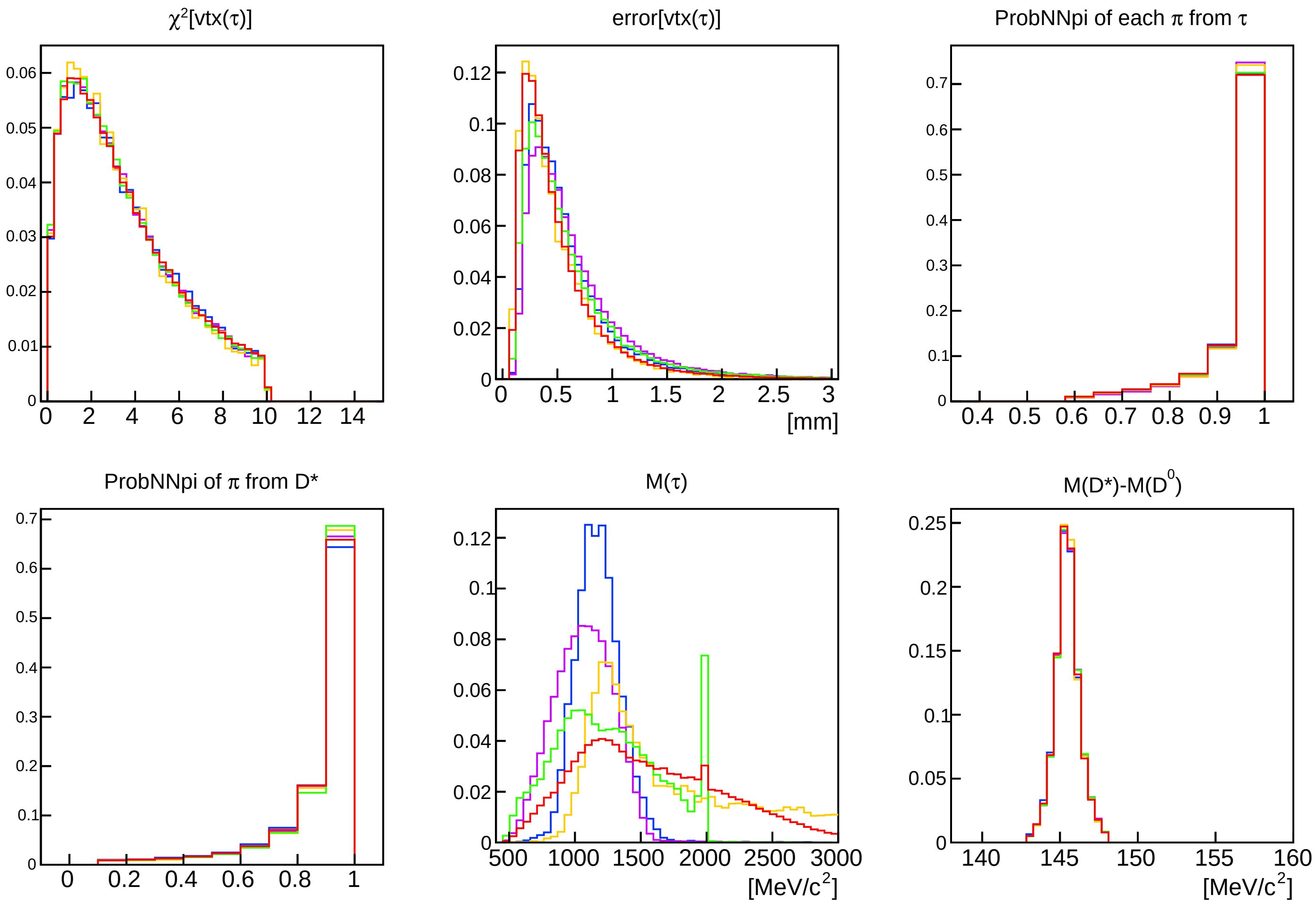

Figure 14: Normalized distribution of various event variables in Run 1 Monte-Carlo samples of signal ($\tau^+ \to 3\pi\overline{\nu}_\tau$ in blue, $\tau^+ \to 3\pi\pi^0\overline{\nu}_\tau$ in purple), normalization (yellow), and background ($B^0 \to D^{*-}D_s^+$ in green, $B^0 \to D^{*-}3\pi X$ in red) events after applying the cleaning cuts.

4.2 Production and validation of 2016 Monte-Carlo samples

Until march 2017, no Monte-Carlo samples had been produced for the $R_{\text{had}}(D^*)$ Run 2 analysis. A first request was formulated on March 22$^{\text{nd}}$ 2017, before the beginning of my internship. It requested large signal samples and smaller normalization samples, in order to compare the gain in efficiency brought by the trigger enhancement between Run 1 and Run 2 and to perform a first comparison with Run 2 data samples. Once the raw samples were created and available on the LHC computing grid [40], I processed the raw datasets using dedicated LHCb software to create Root ntuples [41]. The distributions of some key variables used during the selection are presented on Figure 15. Between Run 1 and Run 2, the center of mass energy of the protons circulating in the LHC almost doubled, increasing the track multiplicity. Also, the LHCb missing energy trigger on hadrons was lowered, so that more events are now selected at small and high momentum, transverse momentum and energy. Figure 15 shows that the resolution on tau-vertex reconstruction improved, as well as the resolution on the invariant mass of the 3π system and the difference of invariant mass between the D^* and the D^0 mesons. The resolution on the tau-vertex error is slightly worse, and the neural network algorithm improved in terms of pion identification. The variables from 2016 samples behave the same way as in Run 1 samples. Therefore the production of the 2016 samples is validated.

An additional set of samples is needed for signal-background comparison. This set has been required on July 27$^{\text{th}}$ 2017. The LHCb collaboration usually limits the size of the produced samples to guarantee the equality of computing resources between each analyses. Therefore these background samples needed to be "filtered" by applying several trigger and pre-selection criteria. This requires to create a dedicated filtering script written in python, determining the features of the pre-selection to be applied. The retention rate R of the script, defined as $R \equiv \frac{\text{N(passed)}}{\text{N(total)}}$ has been evaluated on 2016 Monte-Carlo signal samples to be 2.2%.

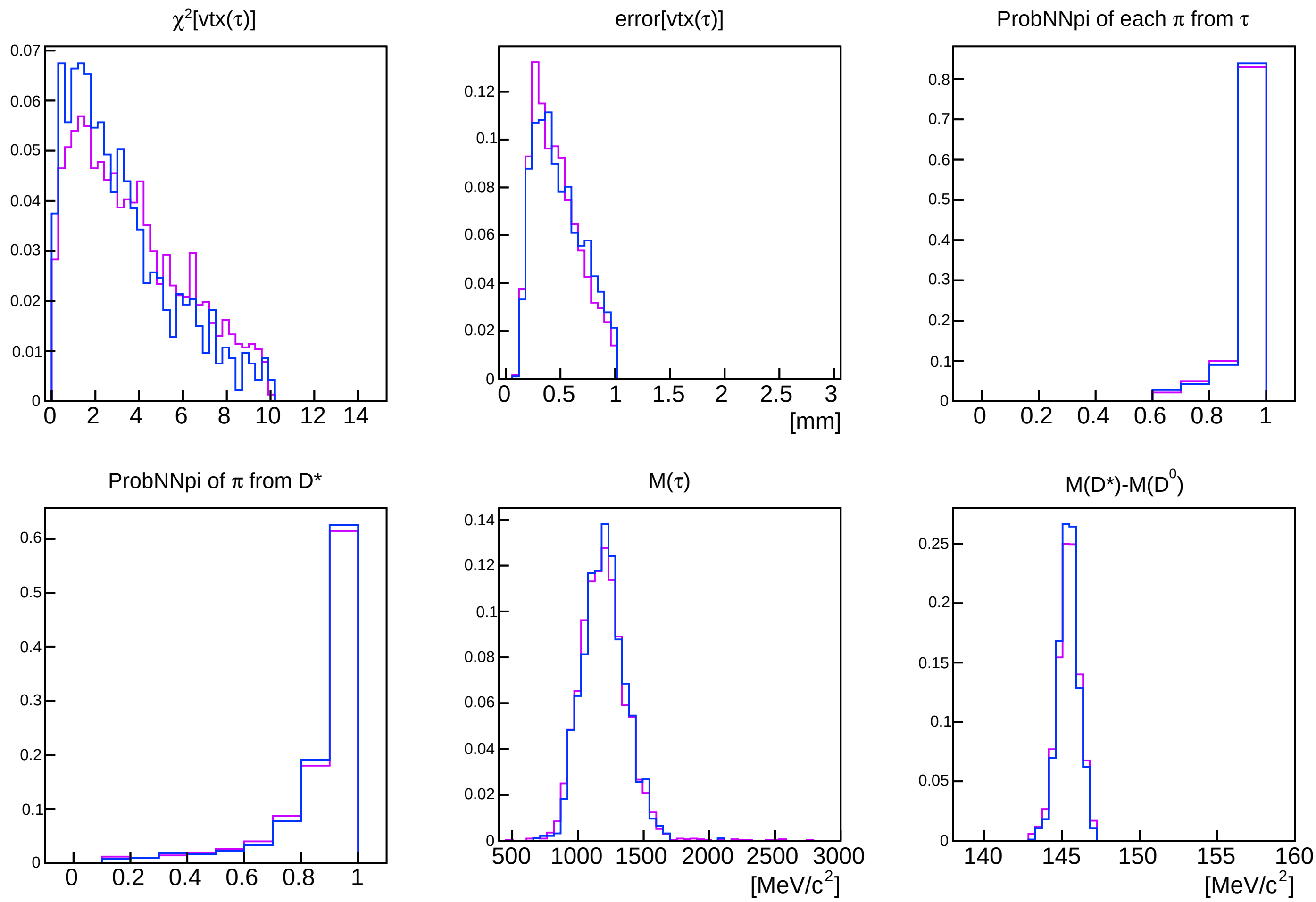

Figure 15: Comparison of various event variables between Run 1 (purple) and Run 2 (blue) signal Monte-Carlo samples. The histograms are normalized to unity.

4.3 Estimation of Run 2 trigger improvements on signal efficiency

The LHCb trigger was redesigned between Run 1 and Run 2, with the introduction of a specific stream, the Turbo stream (Figure 8). The L0 trigger stayed unchanged, but part of the high-level triggers (HLT) is now applied in near real-time and the recording of data

is significantly different from Run 1. In order to compare Run 1 and Run 2 datasets, it is very important to understand and control the conditions under which they were recorded. Only then the event yields can be compared with proper meaning. This is why a detailed comparison of the trigger requirements applied for the creation of each dataset must be performed before any other measurement.
To this end, an overview of the trigger lines used for the Run 1 analysis are detailed in Table 4. Unlike more "classical" analyses which separate the L0, HLT1 and HLT2 levels, the trigger requirements applied to Run 1 datasets for the $R(D^*)$ measurement mix several L0 and HLT2 lines. This is due to the specific features of the $R_{\text{had}}(D^*)$ analysis (*cf.* Section 4.1.2).

Trigger Level	Run 1	Run 2

L0	`B0_L0Global_TIS`
	`Dst_L0HadronDecision_TOS`
	`B0_L0HadronDecision_TOS`
		`B0_L0Global_TIS`
		`Dst_L0HadronDecision_TOS`
		`B0_L0HadronDecision_TOS`

HLT1	`B0_Hlt1TrackAllL0Decision_TOS`	`B0_Hlt1TrackMVADecision_TOS` `B0_Hlt1TwoTrackMVADecision_TOS`

HLT2	`B0_Hlt2Topo2BodyBBDTDecision_TOS`
	`B0_Hlt2Topo3BodyBBDTDecision_TOS`
	`B0_Hlt2Topo4BodyBBDTDecision_TOS`
	`D0_Hlt2CharmHadD02HH_D02KPiDecision_TOS`
		`B0_Hlt2Topo2BodySimpleTDecision_TOS`
		`B0_Hlt2Topo3BodySimpleTDecision_TOS`
		`B0_Hlt2Topo4BodySimpleTDecision_TOS`
		`D0_Hlt2RareCharmD02KPiDecision_Dec`
		`D0_Hlt2CharmHadDstp2D0Pip_D02KmPipTurboDecision_Dec`

Effective combination	`((B0_L0Global_TIS or B0_L0HadronDecision_TOS)`
	`and D0_Hlt2CharmHadD02HH_D02KPiDecision_TOS)`
	`or`
	`(Dst_L0HadronDecision_TOS`
	`and (B0_Hlt2Topo2BodyBBDTDecision_TOS`
	`or B0_Hlt2Topo3BodyBBDTDecision_TOS`
	`or B0_Hlt2Topo4BodyBBDTDecision_TOS))`
		`((B0_L0Global_TIS or B0_L0HadronDecision_TOS)`
		`and (D0_Hlt2RareCharmD02KPiDecision_Dec`
		`or D0_Hlt2CharmHadDstp2D0Pip_D02KmPipTurboDecision_Dec))`
		`or`
		`(Dst_L0HadronDecision_TOS`
		`and (B0_Hlt2Topo2BodyDecision_TOS`
		`or B0_Hlt2Topo3BodyDecision_TOS`
		`or B0_Hlt2Topo4BodyDecision_TOS))`

Table 4: Trigger requirements applied to Run 1 and Run 2 datasets.

In order to optimally minimize the size of the datasets, an additional stage of pre-selection requirements called "stripping" is applied to the triggered data. This stage is performed offline. Stripping is also structured in lines. The stripping of LHCb data is regularly updated to fit the needs of the current analyses, each campaign of stripping being assigned a unique number. The Run 1 analysis uses the `StrippingB2XtauNu` line (which requirements are detailed in appendix B) from the `Stripping21` version. The Run 2 data is produced by applying the `StrippingB0d2DstarTauNuForB2XTauNu` line from `Stripping28`. The HLT1 trigger lines used for Run 1 analysis was applied at the stripping level, making a classical three-level study of the L0, HLT1 and HLT2 impossible. However, it is still possible to determine, in a global way, the efficiency of the overall trigger applied to Run 1 datasets. The adaptation for Run 2 is then performed on a line-by-line basis.
For the L0 trigger, no line has changed. For the HLT1 trigger, the line

B0_Hlt1TrackAllL0Decision_TOS is replaced by the logical "OR" of two new lines using a multivariate algorithm, B0_Hlt1TrackMVADecision_TOS and B0_Hlt1TwoTrackMVADecision_TOS. For the HLT2 trigger, the line D0_Hlt2CharmHadD02HH_D02KPiDecision_TOS has been removed and replaced by the logical "OR" a classical line and a turbo line, D0_Hlt2RareCharmD02KPiDecision_Dec and D0_Hlt2CharmHadDstp2D0Pip_D02KmPipTurboDecision_Dec. Unlike the HLT1 lines which were included to the stripping, the respective efficiency of each HLT2 line can be assessed separately for both Run 1 and Run 2 datasets. These efficiencies are detailed in Figures 16 and 17. The total trigger efficiency for Run 1 is 70.0% and the efficiency for Run 2 is 80.7%. Therefore the relative gain brought to the $R_{\text{had}}(D^*)$ analysis by the trigger improvement between Run 1 and Run 2 is 15.3%.

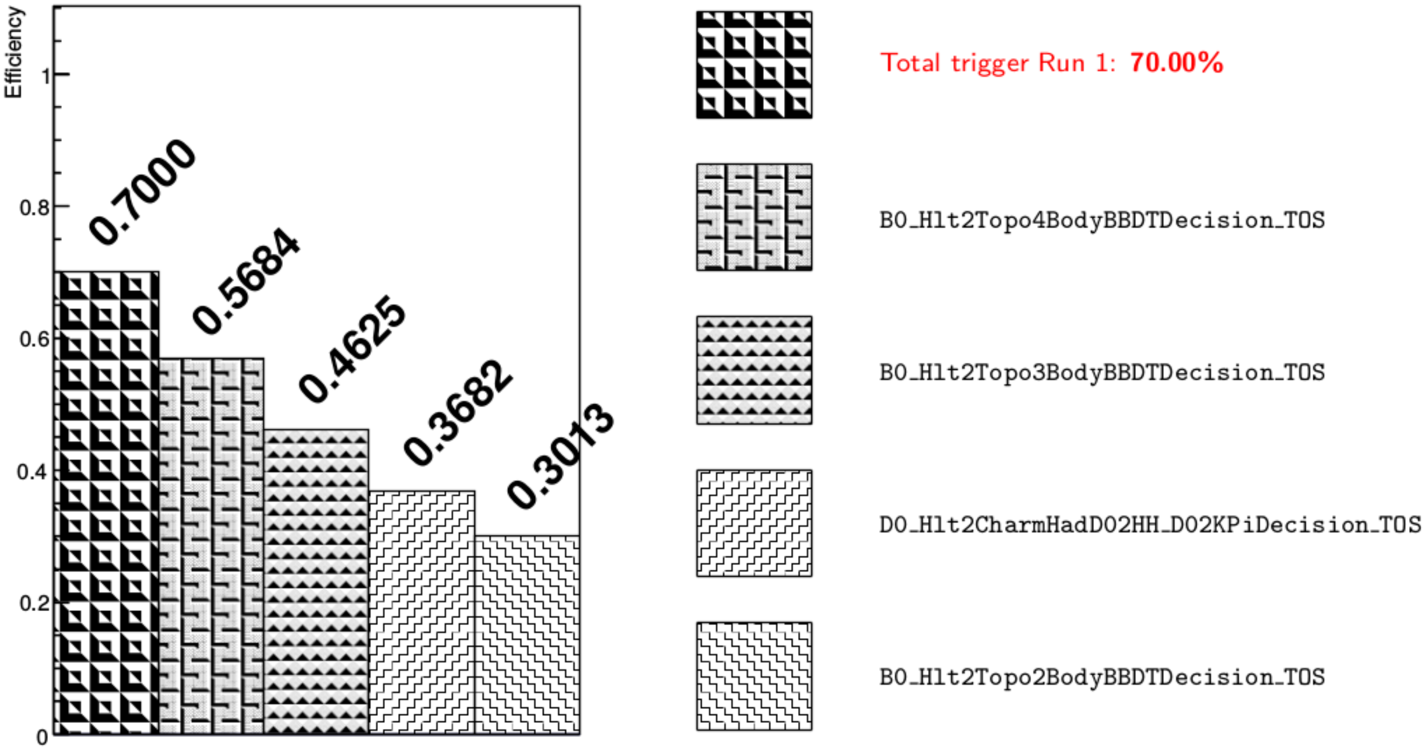

Figure 16: Efficiency of HLT2 trigger lines, evaluated on Run 1 signal Monte-Carlo samples.

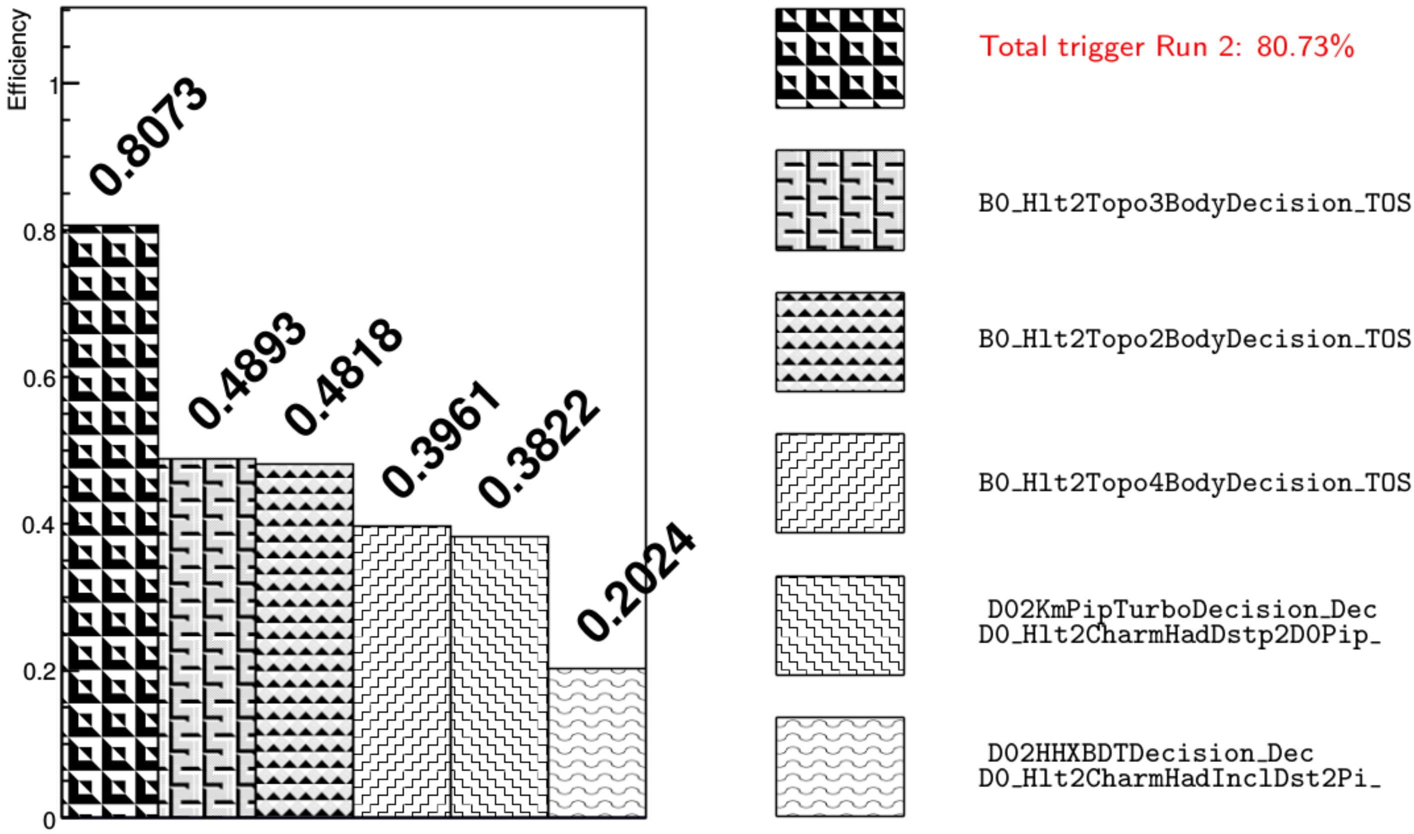

Figure 17: Efficiency of HLT2 trigger lines, evaluated on Run 2 signal Monte-Carlo samples.

4.4 Run 2 gain on background and normalization yields

The $R_{\text{had}}(D^*)$ analysis relies on the original feature that the peaks observed in the invariant mass distribution of various systems (3π, $K^+\pi^-$, *etc.*) are not due to signal but either to normalization or to background events. Whereas the extraction of signal yield requires specific treatment −which was not the subject of this internship− through a three-dimensional fit over non-trivial variables (the transferred 4-momentum to the 3π system, the output of a boosted decision tree and the 3π decay time), this original feature provides a powerful way to estimate both normalization and background yields, and therefore gives a way to assess the statistical gain brought by the enhancements made to the detector for the Run 2 phase. In particular, the topology of the doubly-charmed $B^0 \to D^{*-} D_s^+ (\to \pi^+\pi^-\pi^+)$ background is very similar to the signal mode, thus the estimation of its yield is a direct clue for the improvements that are to be expected for the signal yield. The Run 1 dataset covers the whole Run 1 phase (2011-2012) and the dataset considered for Run 2 actually corresponds to the 2015 year only. The datasets respectively correspond to an integrated luminosity of $3\,\text{fb}^{-1}$ and $0.28\,\text{fb}^{-1}$ of data recorded at the LHC. In order to compare the two periods, the yields are measured per unit of luminosity.

4.4.1 Background yield

The background yield is estimated by fitting the peak produced by doubly-charmed $B^0 \to D^{*-}D_s^+(\to \pi^+\pi^-\pi^+)$ background events in the 3π system mass distribution. These events are isolated from normalization events by requiring an inverted topology, and the 3π invariant mass distribution is fitted around the D_s^+ mass ($1968.28\,\mathrm{MeV}/c^2$). The unbinned likelihood fit is performed using the RooFit toolkit [42]. The probability density function is modelled by a Gaussian function for signal and linear decay for background.

4.4.2 Normalization yield

The normalization yield is estimated by fitting the peak produced by the $B^0 \to D^{*-}\pi^+\pi^-\pi^+$ events in the D^{*-} 3π system mass distribution. The normalization is selected by requiring a normal topology, and the D^{*-} 3π system invariant mass is fitted around the B^0 mass ($\mathrm{m}(B^0) = 5279.63\,\mathrm{MeV}/c^2$). The unbinned likelihood fit is performed using the RooFit toolkit. The probability density function is modelled by a Crystal Ball function [43] for signal and an exponential decay for background.

4.4.3 Fit results

The results of the fit are presented on Figures 6 and 7. The obtained yields are described in Table 5. For the background channel, the number of events per unit luminosity increased from 799 ± 18 (2011-2012) to 2005 ± 96 (2015), so that the Run 2 conditions improve the $B^0 \to D^{*-}D_s^+(\to \pi^+\pi^-\pi^+)$ background yield by a factor 2.51 ± 0.13 with respect to Run 1. For the normalization channel, the number of events per unit luminosity increased from 5861 ± 47 (2011-2012) to 14419 ± 237 (2015), so that the Run 2 conditions improve the $B^0 \to D^*\pi^+\pi^-\pi^+$ normalization yield by a factor 2.46 ± 0.04 with respect to Run 1. Within the precision on this measurement, the gain is independent from the measurement channel, therefore it can be interpreted as originating from the improvements brought by Run 2 conditions of data recording.

Dataset	Integrated luminosity (fb^{-1})	**#Events per $\mathbf{fb}^{-1}$** (Background)	**#Events per $\mathbf{fb}^{-1}$** (Normalization)
Run 1 (2011-2012)	3	799 ± 18	5861 ± 47
Run 2 (2015)	0.28	2005 ± 96	14419 ± 237

Table 5: Result of the fits on the invariant masses (3π system for background, D^{*-} 3π system for normalization) around the D_s^+ (background) and the B^0 (normalization) masses.

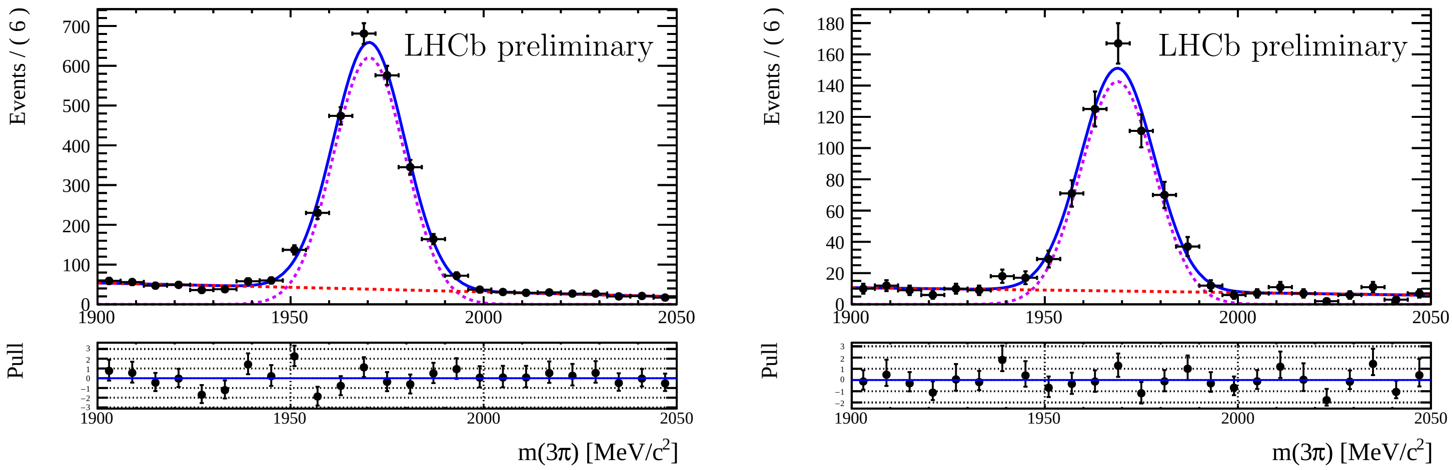

Table 6: Fit to the invariant mass distribution of the 3π system after the vertex inversion requirement, around the D_s^+ mass, for Run 1 (left) and Run 2 (right) datasets.

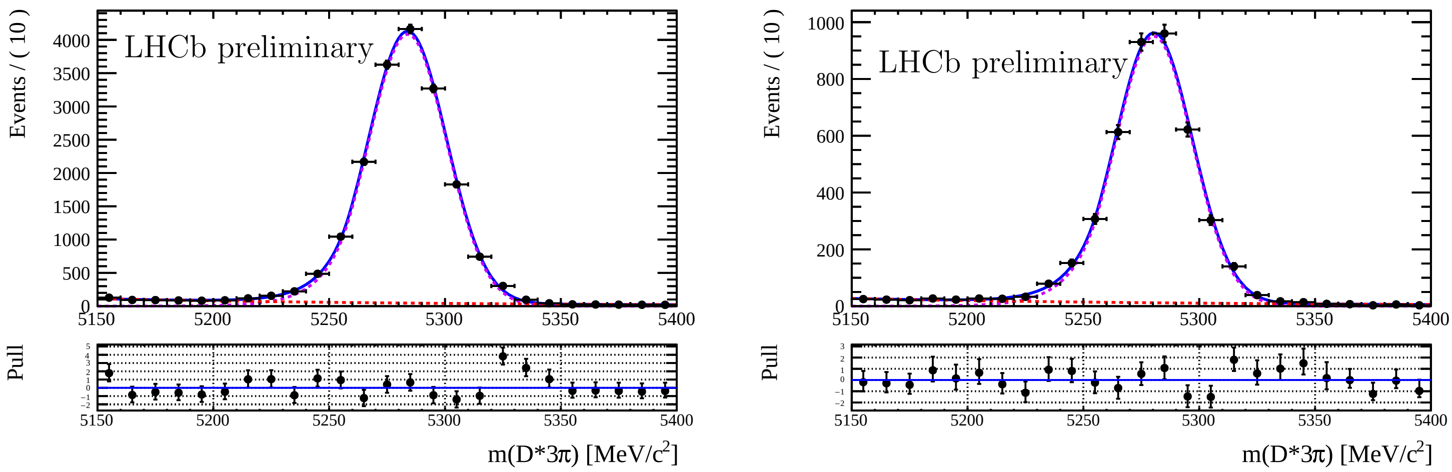

Table 7: Fit to the invariant mass distribution of the D^{*-} 3π system after the vertex inversion requirement, around the B^0 mass, for Run 1 (left) and Run 2 (right) datasets.

5 Conclusion and prospects

The work covered during this internship is the first step towards a measurement of the $R_{\text{had}}(D^*)$ parameter using the full Run 2 dataset recorded at the LHC. This is one of the hottest topics in particle physics nowadays because of the 4.1σ discrepancy observed in the $R(D) - R(D^*)$ world combination with respect to the Standard Model prediction. My work consisted of understanding this discrepancy, learning the general functioning and features of the LHCb detector and studying the analysis performed by the Run 1 team during the past three years. Besides, I have been able to create my own computing tools in object-oriented C++ and python implementations of the LHCb software and the ROOT framework. After validating these tools by with the Run 1 datasets by plotting several variables, analyzing their behaviour and measuring event yields with ROOFIT, I have been able to perform the first look at Run 2 real data and Monte-Carlo samples. This included creating new Monte-Carlo datasets and validating their content, assessing the gain in performance brought by the trigger enhancements made to the LHCb detector between Run 1 and Run 2 and evaluate the gain in statistical precision during the Run 2 period of data recording. This gain comes from three independent factors. First, the center of mass energy increased from $\sqrt{s} = 7\,\text{TeV}$ in 2011 and 2012 to $\sqrt{s} = 13\,\text{TeV}$ since 2015. This factor 1.9 has to be multiplied by the gain in luminosity corresponding to the longer duration of the Run 2 data-taking. The integrated luminosity between 2015 and 2018 is expected to correspond to approximately $6\,\text{fb}^{-1}$ of data, to be compared with the $3\,\text{fb}^{-1}$ recorded between 2011 and 2012. As described above, the improved LHCb trigger brings an additional 15.3% gain. The total expected gain factor is 4.4 and can be compared with the gains measured during this internship. These are expressed in terms of number of events per unit luminosity, so that the gain between Run 1 and Run 2 is measured to be 5.0 ± 0.2. Although this value is higher than the above (naive) expectation, it is of the same order of magnitude. Since the measurement performed in Run 1 data is $R(D^*)[\text{LHCb 2017}] = 0.285 \pm 0.019\,(\text{stat}) \pm 0.025\,(\text{syst}) \pm 0.013\ (\text{BF})$, the future statistical uncertainty on the Run 2 measurement can therefore estimated to be $\sigma_{\text{stat}} = \frac{0.019}{\sqrt{5.0}} = 8.5 \times 10^{-3}$, so that the uncertainty will be dominated by systematics. However, the dominant systematics in the Run 1 measurement was the size of the Monte-Carlo samples used to estimate the background, so that the systematic uncertainties can be decreased either by increasing the size of the Monte-Carlo samples. Besides, the uncertainty brought by the external branching fractions (Eqs. 10 to 12) could also be reduced by more precise measurements. In particular, great expectations are put on the capacity of the Belle II experiment to measure the $B^0 \to D^{*-}\pi^+\pi^-\pi^+$ branching fraction with improved precision. Finally, $R(D^*)$-like measurements can also be performed using other final states involving various types of charmed hadrons ($X_c = D^*$, D^0, D^+, $D_s^{-(*)}$, $\Lambda_c^{+(*)}$, J/ψ, *etc.*). These hadrons differ not only in their masses, but also in their spins. The corresponding $\mathcal{B}(X_b \to X_c\tau^+\nu_\tau)/\mathcal{B}(X_b \to X_c\mu^+\nu_\mu)$ ratios are currently being studied and will allow, hopefully, to disentangle possible scenarii of new physics.

A Fit parameters

The unbinned likelihood fit is performed with floating parameters. The probability density functions are modelled by the following combinations :

- $B^0 \to D^{*-} D_s^+ (\to \pi^+\pi^-\pi^+ X)$ Background : Gaussian for signal, linear decay for background
- $B^0 \to D^{*-}\pi^+\pi^-\pi^+$ Normalization : Crystal Ball [43] for signal, exponential decay for background

The obtained values for the parameters of these functions are taken from the RooFit output. They are listed in Tables 8,10 ($B^0 \to D^{*-} D_s^+ (\to \pi^+\pi^-\pi^+ X)$ background),12 and 14 ($B^0 \to D^{*-}\pi^+\pi^-\pi^+$ normalization). The respective covariance matrices are shown on Tables 9, 11, 13 and 15.

EXT NO.	PARAMETER NAME	VALUE	ERROR	INTERNAL STEP SIZE	INTERNAL VALUE
1	Background	9.22047e+02	3.88635e+01	9.97809e-06	-1.76314e+00
2	Signal	2.39885e+03	5.46546e+01	4.50346e-05	-1.88181e+00
3	coeff_dir	-4.71805e-01	5.66238e-02	4.30109e-06	1.13288e+00
4	m	1.97038e+03	2.20375e-01	1.45456e-04	1.89130e-02
5	ord_orig	1.00156e+03	1.20213e+02	1.94423e-06	-1.37030e+00
6	s	9.25008e+00	1.91647e-01	2.09489e-04	-5.66914e-01

Table 8: Parameters of the fit to the $B^0 \to D^{*-} D_s^+ (\to \pi^+\pi^-\pi^+ X)$ background channel on Run 1 dataset.

PARAMETER NO.	GLOBAL	1	2	3	4	5	6
1	0.38130	1.000	-0.277	0.002	-0.036	0.002	0.315
2	0.31290	-0.277	1.000	-0.001	0.026	-0.001	-0.224
3	0.99817	0.002	-0.001	1.000	-0.003	-0.998	0.001
4	0.10445	-0.036	0.026	-0.003	1.000	-0.003	-0.039
5	0.99817	0.002	-0.001	-0.998	-0.003	1.000	0.001
6	0.34643	0.315	-0.224	0.001	-0.039	0.001	1.000

Table 9: Covariance matrix of the fit to the $B^0 \to D^{*-} D_s^+ (\to \pi^+\pi^-\pi^+ X)$ background channel on Run 1 dataset.

EXT NO.	PARAMETER NAME	VALUE	ERROR	INTERNAL STEP SIZE	INTERNAL VALUE
1	Background	2.07255e+02	1.86812e+01	8.30477e-05	-1.66188e+00
2	Signal	5.65757e+02	2.65985e+01	7.40353e-05	-1.72137e+00
3	coeff_dir	-4.60542e-01	5.67078e-02	1.74937e-04	1.13823e+00
4	m	1.96886e+03	4.67280e-01	5.11348e-04	-5.70670e-02
5	ord_orig	1.01424e+03	1.24894e+02	8.05435e-05	-1.36904e+00
6	s	9.49607e+00	4.13359e-01	7.33756e-04	-5.45458e-01

Table 10: Parameters of the fit to the $B^0 \to D^{*-} D_s^+ (\to \pi^+\pi^-\pi^+ X)$ background channel on Run 2 dataset.

PARAMETER NO.	GLOBAL	1	2	3	4	5	6
1	0.39945	1.000	-0.285	0.013	-0.056	0.013	0.333
2	0.32255	-0.285	1.000	-0.009	0.040	-0.009	-0.234
3	0.95461	0.013	-0.009	1.000	-0.017	-0.954	0.012
4	0.13778	-0.056	0.040	-0.017	1.000	-0.017	-0.087
5	0.95461	0.013	-0.009	-0.954	-0.017	1.000	0.012
6	0.37147	0.333	-0.234	0.012	-0.087	0.012	1.000

Table 11: Covariance matrix of the fit to the $B^0 \to D^{*-} D_s^+ (\to \pi^+\pi^-\pi^+ X)$ background channel on Run 2 dataset.

EXT NO.	PARAMETER NAME	VALUE	ERROR	INTERNAL STEP SIZE	INTERNAL VALUE
1	Alpha	1.49375e+00	8.03277e-02	2.84803e-05	1.49380e-02
2	Background	1.36769e+03	5.95481e+01	3.27253e-04	-1.33636e+00
3	Mean	5.28386e+03	1.58953e-01	1.17145e-03	3.62355e-01
4	Sigma	1.67938e+01	1.39321e-01	1.26716e-03	-8.15761e-01
5	Signal	1.75833e+04	1.40578e+02	3.50866e-04	-5.20852e-01
6	n	3.39384e+01	5.03670e+01	7.32423e-03	-1.30952e+00
7	tau	-6.62694e-03	4.75855e-04	1.37008e-04	1.51930e+00

Table 12: Parameters of the fit to the $B^0 \to D^{*-}\pi^+\pi^-\pi^+$ normalization channel on Run 1 dataset.

PARAMETER NO.	GLOBAL	1	2	3	4	5	6	7
1	0.89380	1.000	-0.133	-0.419	0.468	0.056	-0.795	0.026
2	0.58981	-0.133	1.000	-0.008	-0.194	-0.260	0.366	0.197
3	0.48981	-0.419	-0.008	1.000	-0.335	0.003	0.200	-0.040
4	0.61494	0.468	-0.194	-0.335	1.000	0.082	-0.213	-0.170
5	0.28471	0.056	-0.260	0.003	0.082	1.000	-0.155	-0.084
6	0.87918	-0.795	0.366	0.200	-0.213	-0.155	1.000	-0.104
7	0.34825	0.026	0.197	-0.040	-0.170	-0.084	-0.104	1.000

Table 13: Covariance matrix of the fit to the $B^0 \to D^{*-}\pi^+\pi^-\pi^+$ normalization channel on Run 1 dataset.

EXT NO.	PARAMETER NAME	VALUE	ERROR	INTERNAL STEP SIZE	INTERNAL VALUE
1	Alpha	1.41239e+00	1.02485e-01	8.38772e-07	1.41244e-02
2	Background	3.40696e+02	2.75550e+01	6.39453e-05	-1.45399e+00
3	Mean	5.28044e+03	3.31003e-01	7.31590e-05	2.19540e-01
4	Sigma	1.66350e+01	2.93941e-01	2.09909e-04	-8.25077e-01
5	Signal	4.06730e+03	6.69766e+01	2.45613e-05	-1.08390e+00
6	n	1.49246e+02	1.02492e+03	8.56904e-04	-1.01742e+00
7	tau	-6.24347e-03	9.19280e-04	2.16775e-05	1.52082e+00

Table 14: Parameters of the fit to the $B^0 \to D^{*-}\pi^+\pi^-\pi^+$ normalization channel on Run 2 dataset.

PARAMETER NO.	GLOBAL	1	2	3	4	5	6	7
1	0.75120	1.000	0.171	-0.458	0.525	-0.070	-0.397	-0.100
2	0.48810	0.171	1.000	-0.072	-0.141	-0.227	0.140	0.200
3	0.49278	-0.458	-0.072	1.000	-0.342	0.030	0.066	-0.008
4	0.62352	0.525	-0.141	-0.342	1.000	0.058	-0.070	-0.193
5	0.24697	-0.070	-0.227	0.030	0.058	1.000	-0.058	-0.082
6	0.53190	-0.397	0.140	0.066	-0.070	-0.058	1.000	-0.048
7	0.31131	-0.100	0.200	-0.008	-0.193	-0.082	-0.048	1.000

Table 15: Covariance matrix of the fit to the $B^0 \to D^{*-}\pi^+\pi^-\pi^+$ normalization channel on Run 2 dataset.

B Stripping requirements

Cut	Value
B^0	
$m(D^*\pi\pi\pi)$	2500-5600 MeV/c^2
DIRA	> 0.995 (0.999)
Max. DOCA	< 0.15 mm
D^*	
p_T	> 1250 MeV/c
Vertex χ^2/DOF	< 25
$m(D^* - D^0)$	135-150 MeV/c^2
$m(D^0\pi)$	1960-2060 MeV/c^2
D^0	
p_T	> 1600 MeV/c
Vertex Distance χ^2	> 50
DIRA	> 0.999
Vertex χ^2/DOF	< 10
$m(K\pi)$	1825-1905 MeV/c^2
Max. DOCA	< 0.5 mm
Max. DOCA χ^2	< 15
τ	
m($\pi\pi\pi$)	400-3500 MeV/c^2
min[m($\pi\pi$)]	< 1670 MeV/c^2
DIRA	> 0.99
Vertex χ^2	< 25
Max. DOCA	< 0.15 mm
At least two pions p_T	> 300 MeV/c^2
At least two pions IP χ^2	> 5
τ daughter pions	
p_T	> 250 MeV/c
IP χ^2	> 4
Track χ^2/DOF	< 3
PIDK	< 8
Ghost probability	< 0.4
D^0 daughters	
p_T	> 250 MeV/c
p	> 2000 MeV/c
$p_T(K) + p_T(\pi)$	> 1200 MeV/c
Kaon PIDK	$>$ -5
Pion PIDK	< 8
Track χ^2/DOF	< 3
IP χ^2	> 4
Ghost Probability	< 0.4
Slow Pion	
p_T	> 110 MeV/c
Track χ^2/DOF	< 3
Ghost Probability	< 0.6

Table 16: Cuts used in the stripping selection of Run 1 dataset [8].

C List of the main datasets/Monte-Carlo samples, Git repository

C.1 Run 1

All Run 1 samples are stored on LHCb server at CPPM. The generic path for the samples is `/lhcb5/zfs_lhcb/users/arbouch/fbetti/BtoDsttaunu/mergedAll/`

- Signal Monte-Carlo $B^0 \to D^{*}\tau^{+}\nu_{\tau}$ with $\tau^{+} \to \pi^{+}\pi^{-}\pi^{+}\overline{\nu}_{\tau}$:
  - `MC/aug_sig3piTauolaBaBar_11160001_MC11_DecayTree_only_cleaning_merged.root`
  - `MC/aug_sig3piTauolaBaBar_11160001_MC12_DecayTree_only_cleaning_merged.root`
- Signal Monte-Carlo $B^0 \to D^{*}\tau^{+}\nu_{\tau}$ with $\tau^{+} \to \pi^{+}\pi^{-}\pi^{+}\pi^{0}\overline{\nu}_{\tau}$:
  - `MC/aug_sig3pipi0Tauola_11563020_MC11_DecayTree_only_cleaning_merged.root`
  - `MC/aug_sig3pipi0Tauola_11563020_MC12_DecayTree_only_cleaning_merged.root`
- Normalization Monte-Carlo $B^0 \to D^{*}\pi^{+}\pi^{-}\pi^{+}$:
  - `MC/aug_B0Dst3piNoGen_11266018_MC11_DecayTree_only_cleaning_merged.root`
  - `MC/aug_B0Dst3piNoGen_11266018_MC12_DecayTree_only_cleaning_merged.root`
- Background Monte-Carlo $B^0 \to D^{*}\pi^{+}\pi^{-}\pi^{+}X$:
  - `MC/aug_inclDst3piAcc_27163000_MC11_DecayTree_only_cleaning_merged.root`
  - `MC/aug_inclDst3piAcc_27163000_MC12_DecayTree_only_cleaning_merged.root`
- Background Monte-Carlo $B^0 \to D^{*}D_s^{+}$ with $D_s^{+} \to \pi^{+}\pi^{-}\pi^{+}X$, D_s^{+} up to 3-prong:
  - `MC/aug_DstDs_11696610_MC11_DecayTree_only_cleaning_merged.root`
  - `MC/aug_DstDs_11696610_MC12_DecayTree_only_cleaning_merged.root`
- Background Monte-Carlo $B^0 \to D^{*}D_s^{+}$ with $D_s^{+} \to \pi^{+}\pi^{-}\pi^{+}X$, D_s^{+} up to 5-prong:
  - `MC/aug_DstDs5Trk_11896410_MC11_DecayTree_only_cleaning_merged.root`
  - `MC/aug_DstDs5Trk_11896410_MC11_DecayTree_only_cleaning_merged.root`
- 2011 and 2012 datasets :
  - `data/aug_data_2011_DecayTree_only_cleaning_merged.root`
  - `data/aug_data_2012_DecayTree_only_cleaning_merged.root`

C.2 Run 2

All Run 2 samples are stored on LHCb server at CPPM. The Monte-Carlo samples were generated by me with the `DecayTreeTuple` toolkit from the `DaVinci` software developed within the LHCb collaboration. The generic path for the samples is `/lhcb5/zfs_lhcb/users/arbouch/Olivier/`

- Signal Monte-Carlo $B^0 \to D^{*}\tau^{+}\nu_{\tau}$ with $\tau^{+} \to \pi^{+}\pi^{-}\pi^{+}\overline{\nu}_{\tau}$:
  - `sig3piTauolaBaBar_11160001_MC16_MagDown_DecayTree.root`
  - `sig3piTauolaBaBar_11160001_MC16_MagUp_DecayTree.root`
- Signal Monte-Carlo $B^0 \to D^{*}\tau^{+}\nu_{\tau}$ with $\tau^{+} \to \pi^{+}\pi^{-}\pi^{+}\pi^{0}\overline{\nu}_{\tau}$:
  - `sig3pipi0Tauola_11563020_MC16_MagDown_DecayTree.root`
  - `sig3pipi0Tauola_11563020_MC16_MagUp_DecayTree.root`
- Normalization Monte-Carlo $B^0 \to D^{*}\pi^{+}\pi^{-}\pi^{+}$:
  - `B0Dst3piNoGen_11266018_MC16_MagDown_DecayTree.root`
  - `B0Dst3piNoGen_11266018_MC16_MagUp_DecayTree.root`
- 2015 datasets (`/lhcb5/zfs_lhcb/users/arbouch/AntonioSantiago/b2Xctaunu/B02Dsttaunu/Ntuples/AfterSelection/v0/`):
  - `data_B02DstTauNu_2015_magDown_Job98_selection_vars.root`
  - `data_B02DstTauNu_2015_magUp_Job97_selection_vars.root`

C.3 Git repository

The latest version of my code is available on the gitlab repository of the $R_{\mathrm{had}}(X_c)$ sub-working group :

https://gitlab.cern.ch/oleroy/RXc_had/RDstar_had_Emmanuel

This includes the ROOT tuples maker, the filtering script for 2016 Monte-Carlo production as well as the python macros for plotting, fitting and computing trigger efficiencies.

D Cut dictionnary

Selection	Name in the `cuts_taugw_new.cc` Root macro
Cleaning cuts	`final_light`
Inverted topology	`basic_ant4`
Normal topology	`normal`
Trigger Run 1	`trigOR+Trigalltopo+!nol0`
Fitting	`normal_final_ana` (normalization-like topologies) `final_ana` (inverted topologies)

Table 17: Name of the main selection requirements used by the Run 1 analysis team in their Root macros.

References

[1] DELPHI, OPAL, ALEPH, LEP Electroweak Working Group, L3, L. DELPHI/OPAL/ALEPH/LEP Electroweak Working Group, *A Combination of preliminary electroweak measurements and constraints on the standard model*, arXiv:hep-ex/0511027.

[2] S. Fajfer, J. F. Kamenik, and I. Nisandzic, *On the $B \to D^* \tau \bar{\nu}_\tau$ Sensitivity to New Physics*, Phys. Rev. **D85** (2012) 094025, arXiv:1203.2654.

[3] BaBar, J. P. Lees *et al.*, *Evidence for an excess of $\bar{B} \to D^{(*)} \tau^- \bar{\nu}_\tau$ decays*, Phys. Rev. Lett. **109** (2012) 101802, arXiv:1205.5442.

[4] Belle, M. Huschle *et al.*, *Measurement of the branching ratio of $\bar{B} \to D^{(*)} \tau^- \bar{\nu}_\tau$ relative to $\bar{B} \to D^{(*)} \ell^- \bar{\nu}_\ell$ decays with hadronic tagging at Belle*, Phys. Rev. **D92** (2015), no. 7 072014, arXiv:1507.03233.

[5] LHCb, R. Aaij *et al.*, *Measurement of the ratio of branching fractions $\mathcal{B}(\bar{B}^0 \to D^{*+} \tau^- \bar{\nu}_\tau)/\mathcal{B}(\bar{B}^0 \to D^{*+} \mu^- \bar{\nu}_\mu)$*, Phys. Rev. Lett. **115** (2015), no. 11 111803, arXiv:1506.08614, [Erratum: Phys. Rev. Lett.115,no.15,159901(2015)].

[6] Belle, Y. Sato *et al.*, *Measurement of the branching ratio of $\bar{B}^0 \to D^{*+} \tau^- \bar{\nu}_\tau$ relative to $\bar{B}^0 \to D^{*+} \ell^- \bar{\nu}_\ell$ decays with a semileptonic tagging method*, Phys. Rev. **D94** (2016), no. 7 072007, arXiv:1607.07923.

[7] Belle, S. Hirose *et al.*, *Measurement of the τ lepton polarization and $R(D^*)$ in the decay $\bar{B} \to D^* \tau^- \bar{\nu}_\tau$*, Phys. Rev. Lett. **118** (2017), no. 21 211801, arXiv:1612.00529.

[8] LHCb collaboration, F. Betti *et al.*, *Measurement of $B^0 \to D^{*-} \tau^+ \nu_\tau$ with tau three-prong decays* , LHCb-ANA-2015-045. Internal note.

[9] Y. Amhis *et al.*, *Averages of b-hadron, c-hadron, and τ-lepton properties as of summer 2016*, arXiv:1612.07233, updated results and plots available at http://www.slac.stanford.edu/xorg/hfag/.

[10] A. Crivellin, C. Greub, and A. Kokulu, *Explaining $B \to D\tau\nu$, $B \to D^*\tau\nu$ and $B \to \tau\nu$ in a 2HDM of type III*, Phys. Rev. **D86** (2012) 054014, arXiv:1206.2634.

[11] Y. Sakaki, M. Tanaka, A. Tayduganov, and R. Watanabe, *Testing leptoquark models in $\bar{B} \to D^{(*)} \tau \bar{\nu}$*, Phys. Rev. **D88** (2013), no. 9 094012, arXiv:1309.0301.

[12] Y. Sakaki, M. Tanaka, A. Tayduganov, and R. Watanabe, *Probing New Physics with q^2 distributions in $\bar{B} \to D^{(*)} \tau \bar{\nu}$*, Phys. Rev. **D91** (2015), no. 11 114028, arXiv:1412.3761.

[13] D. Beirevi, S. Fajfer, N. Konik, and O. Sumensari, *Leptoquark model to explain the B-physics anomalies, R_K and R_D*, Phys. Rev. **D94** (2016), no. 11 115021, arXiv:1608.08501.

[14] BaBar, J. P. Lees *et al.*, *Measurement of an Excess of $\bar{B} \to D^{(*)} \tau^- \bar{\nu}_\tau$ Decays and Implications for Charged Higgs Bosons*, Phys. Rev. **D88** (2013), no. 7 072012, arXiv:1303.0571.

[15] LHCb, R. Aaij *et al.*, *Test of lepton universality using $B^+ \to K^+\ell^+\ell^-$ decays*, Phys. Rev. Lett. **113** (2014) 151601, arXiv:1406.6482.

[16] Belle, S. Wehle *et al.*, *Lepton-Flavor-Dependent Angular Analysis of $B \to K^*\ell^+\ell^-$*, Phys. Rev. Lett. **118** (2017), no. 11 111801, arXiv:1612.05014.

[17] A. Abdesselam *et al.*, *Measurement of the τ lepton polarization in the decay $\bar{B} \to D^*\tau^-\bar{\nu}_\tau$*, arXiv:1608.06391.

[18] D. Bigi and P. Gambino, *Revisiting $B \to D\ell\nu$*, Phys. Rev. **D94** (2016), no. 9 094008, arXiv:1606.08030.

[19] BaBar, J. P. Lees *et al.*, *Measurement of the $B^0 \to D^{*-}\pi^+\pi^-\pi^+$ branching fraction*, Phys. Rev. **D94** (2016), no. 9 091101, arXiv:1609.06802.

[20] Particle Data Group, C. Patrignani *et al.*, *Review of Particle Physics*, Chin. Phys. **C40** (2016), no. 10 100001.

[21] LHCb collaboration, A. A. Alves Jr. *et al.*, *The LHCb detector at the LHC*, JINST **3** (2008) S08005.

[22] R. Aaij *et al.*, *Performance of the LHCb Vertex Locator*, JINST **9** (2014) P09007, arXiv:1405.7808.

[23] R. Arink *et al.*, *Performance of the LHCb Outer Tracker*, JINST **9** (2014) P01002, arXiv:1311.3893.

[24] M. Adinolfi *et al.*, *Performance of the LHCb RICH detector at the LHC*, Eur. Phys. J. **C73** (2013) 2431, arXiv:1211.6759.

[25] P. Perret, *First Years of Running for the LHCb Calorimeter system*, LHCb-PROC-2014-017.

[26] A. A. Alves Jr. *et al.*, *Performance of the LHCb muon system*, JINST **8** (2013) P02022, arXiv:1211.1346.

[27] R. Aaij *et al.*, *The LHCb trigger and its performance in 2011*, JINST **8** (2013) P04022, arXiv:1211.3055.

[28] G. Dujany and B. Storaci, *Real-time alignment and calibration of the LHCb Detector in Run II*, J. Phys. Conf. Ser. **664** (2015) 082010.

[29] R. Aaij *et al.*, *Tesla: an application for real-time data analysis in High Energy Physics*, Comput. Phys. Commun. **208** (2016) 35, arXiv:1604.05596.

[30] B. Sciascia, *LHCb Run 2 Trigger Performance*, LHCb-PROC-2016-020.

[31] T. Sjöstrand, S. Mrenna, and P. Skands, *PYTHIA 6.4 physics and manual*, JHEP **05** (2006) 026, arXiv:hep-ph/0603175; T. Sjöstrand, S. Mrenna, and P. Skands, *A brief introduction to PYTHIA 8.1*, Comput. Phys. Commun. **178** (2008) 852, arXiv:0710.3820.

[32] I. Belyaev *et al.*, *Handling of the generation of primary events in Gauss, the LHCb simulation framework*, J. Phys. Conf. Ser. **331** (2011) 032047.

[33] D. J. Lange, *The EvtGen particle decay simulation package*, Nucl. Instrum. Meth. **A462** (2001) 152.

[34] P. Golonka and Z. Was, *PHOTOS Monte Carlo: A precision tool for QED corrections in Z and W decays*, Eur. Phys. J. **C45** (2006) 97, `arXiv:hep-ph/0506026`.

[35] Geant4 collaboration, J. Allison *et al.*, *Geant4 developments and applications*, IEEE Trans. Nucl. Sci. **53** (2006) 270; Geant4 collaboration, S. Agostinelli *et al.*, *Geant4: A simulation toolkit*, Nucl. Instrum. Meth. **A506** (2003) 250.

[36] M. Clemencic *et al.*, *The LHCb simulation application, Gauss: Design, evolution and experience*, J. Phys. Conf. Ser. **331** (2011) 032023.

[37] LHCb, R. Aaij *et al.*, *A precise measurement of the B^0 meson oscillation frequency*, Eur. Phys. J. **C76** (2016), no. 7 412, `arXiv:1604.03475`.

[38] A. Hoecker *et al.*, *TMVA - Toolkit for Multivariate Data Analysis*, ArXiv Physics e-prints (2007) `arXiv:physics/0703039`.

[39] V. V. Gligorov and M. Williams, *Efficient, reliable and fast high-level triggering using a bonsai boosted decision tree*, JINST **8** (2013) P02013, `arXiv:1210.6861`.

[40] C. Eck *et al.*, *LHC computing Grid: Technical Design Report. Version 1.06 (20 Jun 2005)*, Technical Design Report LCG, CERN, Geneva, 2005.

[41] R. Brun and F. Rademakers, *ROOT: An object oriented data analysis framework*, Nucl. Instrum. Meth. **A389** (1997) 81.

[42] W. Verkerke and D. P. Kirkby, *The RooFit toolkit for data modeling*, eConf **C0303241** (2003) MOLT007, `arXiv:physics/0306116`, [,186(2003)].

[43] T. Skwarnicki, *A study of the radiative cascade transitions between the Upsilon-prime and Upsilon resonances*, PhD thesis, Institute of Nuclear Physics, Krakow, 1986, DESY-F31-86-02.